The Role of Magma Storage Conditions and Excess Fluids in the Effusive to Explosive Eruption Styles

Sri Budhi Utami[1]*, Juan Andùjar[2], Fidel Costa[1,3], Bruno Scaillet[2], and Hanik Humaida[4]

[1] Asian School of the Environment, Nanyang Technological University, 50 Nanyang Avenue, N2-01B-27, Singapore, 639798.

[2] Institut des Sciences de la Terre Orléans (ISTO), CNRS-Université d'Orléans-BRGM, 1A Rue de la Ferrollerie, 45100, Orléans, France.

[3] Earth Observatory of Singapore, 50 Nanyang Avenue, N2-01A-15, Singapore, 639798.
ORCiD:

[4] Balai Penyelidikan dan Perkembangan Teknologi Kebencanaan Geologi, Jalan Cendana, 15, D.I. Yogyakarta, Indonesia

*Corresponding author: Sri Budhi Utami (sri.budhi.utami@gmail.com).

Key Points:

- We use phase equilibria experiments to evaluate the role of magmatic storage conditions on eruption style of Kelud volcano, Indonesia.
- Explosive eruptions retain an excess fluid phase, whereas the lava dome lose this phase gradually; both share similar storage conditions.
- The accumulation of fluids could lead to decreasing magma density over time, which could be monitored using gravity measurements.

Abstract

We investigate the role of pre-eruptive magma conditions in controlling eruption styles at basaltic andesite volcanoes, and their relationship to monitoring data. We focus on a cycle of explosive (1990, sub-Plinian) → effusive (2007 dome) → explosive (2014, sub-Plinian) eruptions at Kelud volcano, Indonesia. We conducted petrological analyses of eruption products and phase equilibria experiments using a pumice from the 1990 eruption across a wide range of conditions (temperature, pressure, oxygen fugacity, and volatile contents). We are able to reproduce the main mineral assemblage of all three magmas (plagioclase + pyroxenes + amphibole + olivine + magnetite) at T = 975 ± 39°C, P = 175 ± 25 MPa, fO_2 = NNO, and 4-6 wt. % water in the melt, which is also consistent with the phenocryst contents for explosive eruptions (30-50 wt. %). The high phenocryst content of the 2007 dome (~ 70 wt. %) implies a lower volatile content (~1 wt. % water in the melt), which likely resulted from slow magma ascent towards the surface alongside progressive equilibration. Mass balance calculations on the sulfur budget of the 1990 and 2014 magmas, show that they contained an excess fluid phase that was stored with the magma, and we propose that this led to their more explosive eruption style compared to the 2007 dome. Our hypothesis of accumulation of excess fluids could perhaps be recorded as changes in gravity data over time, and may open doors to better anticipate eruption styles.

Plain Language Summary

Many volcanoes can erupt explosively or grow lava domes, and it is still difficult to know how and when the volcano may erupt in the future. We use experiments to investigate whether the temperature, pressure, and dissolved gas content of eruptible molten rock underneath a volcano can control its eruption style, and then relate them to monitoring data signals typically used to anticipate eruptions. We also study rocks from the 1990-2014 eruptions of Kelud volcano in Indonesia, which is notorious for its explosive and short eruptions, but can also shifts to lava dome growth. We find that the depth, temperature and gases dissolved in the melt are essentially the same for the 2007 lava dome, and the 1990 and 2014 explosive eruptions. However, explosive eruptions also accumulate a separate surplus gas phase before eruption (e.g. “pressure cooker” effect), whereas before lava dome growth this gas phase is lost over time to the surface.

Thus it may be possible to anticipate eruption styles by tracking the gravity and density changes below the volcano.

1 Introduction

Volcanoes can display a range of eruption styles, spanning from small phreatic events, to dome growth, or explosive events with tall eruptive columns. Such changes can occur between consecutive eruptions of the same volcano, and even within a single eruption. Some well-known examples of volcanoes that display large variations in eruptive styles between eruptions, include Merapi (Indonesia e.g. Surono et al., 2012), Soufrière Hills (Montserrat; e.g. Young et al., 1998), and Mt. St Helens (USA; e.g. Pallister et al., 1992). Examples of how a single volcanic eruption can also rapidly transition from effusive to explosive and vice versa were observed in the 1991 Pinatubo eruption (Bernard et al., 1996; Pallister et al., 1996), the 2009 eruption at Redoubt (Bull & Buurman, 2013), or the 2011 eruption at Puyehue-Cordón Caulle (Elissondo et al., 2016). The changes in eruptive style are typically abrupt and difficult to anticipate, which makes the mitigation of associated hazards incredibly challenging.

Changes in eruptive styles are largely controlled by the physical and chemical properties of the magmas at their storage zones, and how these change as the magma ascends towards the surface and goes through the brittle-ductile transition (e.g. Cashman et al., 2013; Dingwell et al., 1993). Some parameters include the pre-eruptive magmatic storage pressure, temperature, crystallinity, melt composition and magmatic volatile contents. The pre-eruptive volatile content of the melt is especially important in determining key parameters, namely the viscosity, buoyancy, and magma ascent rate (Cassidy et al., 2018; Giordano et al., 2008; Gonnermann & Manga, 2013). In addition, the presence of an exsolved volatile phase at the pre-eruptive system due to second boiling (Sisson & Bacon, 1999) or volatile flushing (Caricchi et al., 2018) can also have a large impact on eruption dynamics. Moreover, such exsolved fluid phase has been documented and quantified for many explosive eruptions (Scaillet et al., 1998). Nothwithstanding our understanding of the parameters and processes leading to explosive eruptions it is still very challenging to anticipate whether a given volcano will erupt explosively or effusively (Cassidy et al., 2018; Shinohara, 2008).

In this study, we investigate the pre-eruptive conditions and processes that may have led to a sequence of explosive-effusive-explosive eruption of Kelud volcano (Indonesia), as exemplified by the 1990 → 2007 → 2014 eruptions. We also report new petrological observations that we combine with various mineral-melt geothermobarometers, and new phase equilibria experiments to constrain the pre-eruptive storage conditions of the three eruptions. The combined petrological and experimental results suggest that the magma that fed the 1990, 2007, and 2014 events were essentially stored at similar temperatures, pressures, and fO_2 range. We propose that the higher explosivity of the 1990 and 2014 eruptions was instead driven by the presence of exsolved volatile phase that was lacking in the 2007 dome eruption, and this led to slower ascent, enhanced degassing, and subsequent re-equilibration of the magma towards the surface that ultimately produced a dome.

2 Geological Setting

2.1 Kelud volcano

Kelud (Kelut) volcano is an active basaltic-andesite semi-plugged composite strato-cone complex situated in East Java, Indonesia (Whelley et al., 2015; Wirakusumah, 1991). The volcano hosts a persistent crater lake fed by meteoric water (neutral pH) during repose, and explosive eruptions typically generate syn-eruptive and post-eruptive cold lahars (Thouret et al., 1998). Kelud typically generates short-lived explosive eruptions with run-up times of mere hours (Global Volcanism Program, 2013; Lesage & Surono, 1995; Maeno et al., 2019). Kelud has erupted at least 32 times in the last 100 years (Global Volcanism Program, 2013), but here we focus on the last three eruptions in 1990, 2007, and 2014.

The 1990 explosive eruption began after ~3 months of unrest followed by quiescence for ~3 weeks (Bourdier et al., 1997). Escalation towards eruption occurred in hours, giving communities only one hour to evacuate their homes (Global Volcanism Program, 1990a). The explosive eruption of 2014 largely followed a similar pattern in terms of duration of heightened unrest and steep increase in seismicity hours to days before the eruption (Hidayati et al., 2018). These 1990 and 2014 events generated eruptive columns as high as 17 km (Bourdier et al., 1997;

Kristiansen et al., 2015; Nakashima et al., 2016) with a VEI of 4 and Dense Rock Equivalent (DRE) volumes of 6.3 x 10^7 m^3 (1990) and 2.1 x 10^8 m^3 (2014), respectively (Maeno et al., 2019). Moreover, the eruptions were short-lived and volcanic activity and unrest returned to background levels within days to weeks of the main eruptive phase (Global Volcanism Program, 2014; Pardyanto, 1990).

The lava dome extrusion of November 2007 and was preceded by unrest that started as early as January 2007, according to Lubis (2014) who detected up to 11 cm inflation around the summit region from remote sensing data. From July to August 2007 unrest involved intense degassing on the lake floor and increase in seismicity (Hidayati et al., 2018) and lake temperature rising up (from ~30°C to ~75°C), as well as heightened CO_2 emissions from the lake (Caudron et al., 2012; Global Volcanism Program, 2007; Hidayati et al., 2009; Kunrat, 2009). Continuous seismic unrest started around September 2007, involving multiple swarms and low frequency earthquakes (Hidayati et al., 2009). The seismic unrest was further accompanied by inflation from 9th October until 3rd November, when the signal changed to deflation and gave way to slow dome extrusion (Hidayati et al., 2018). The final dome was 200 m high and 400 m wide, with a volume of 3.5 x 10^7 m^3 which is about half the volume of the 1990 eruption, but about one order of magnitude smaller than the 2014 event (Global Volcanism Program, 2008; Maeno et al., 2019).

3 Materials and Methods

We performed petrological analyses of two 2007 dome fragments previously studied in Humaida (2013), and two pumices sampled following the 2014 eruption (sampled by H. Humaida), and also include the data from the six main-stage pumices from the 1990 eruption (already studied in Utami et al., in revision). We chose one basaltic andesite pumice from the 1990 eruption (KELUD1990-PL1 or PL1 from Utami et al. (in revision)) as the starting material for experiments, because it was the most mafic, and had the same mineral assemblage of the other samples except for the absence of olivine.

3.1 Selection of experimental conditions

145 We experimentally investigated a range of variables that includes previous estimates
146 from mineral-melt geothermobarometers (Utami et al., in revision). We varied temperature from
147 950 to 1060°C, pressure from 100 to 400 MPa, fO_2 at the Ni-NiO buffer (NNO) and up to two
148 log units above (NNO + 2), and varied a volatile composition in the capsule from pure water to
149 pure CO_2 (See below for more details).
150

151 3.2 Preparation of experimental charges

152 A starting glass was prepared by finely crushing the pumice using a ceramic mortar and
153 pestle, and homogenized by fusing the powder at 1400°C and at atmospheric pressure for around
154 6 hours in a standard Thermconcept furnace at 1750°C. EPMA analyses of the fused glass
155 confirmed that glass it was homogenous, and of the same composition as the whole rock (Table
156 1). This glass was crushed again to a fine dry powder with an agate mortar and pestle, and was
157 used as starting material for all experiments. About 0.03g of dry glass was loaded in Au capsules
158 (of size 10-15 mm x 2.5 x 0.2 mm wall thickness) for the 950°C and 1000°C experiments,
159 whereas Au-Pd capsules were used for the 1060°C experiments.
160

161 We varied the fluid composition (referred to as XH_2O_{in} = initial H_2O / [H_2O + CO_2] in
162 moles) from 0 to 1 by adding various amounts of deionized water and CO_2 (in the form of silver
163 oxalate) to the dry glass powder according to the methodology of Scaillet et al. (1995). All the
164 successful runs were fluid saturated. The capsules were arc-welded and weighed before being
165 stored in a 60°C oven to homogenize the fluid content for 6-12 hours. After each experiments,
166 the capsule was re-weighed again to check for fluid loss during storage and subsequent
167 experiments. To determine whether the charges were properly sealed, their weight had to be
168 within 0.0005 g of the original value, which was the precision of the analytical balance. We
169 observed that capsules from successfully quenched experiments were shrunk and flattened but
170 had the same weight as before the experiment. Upon opening the charges ejected gas with an
171 audible pop. In contrast, failed charges appeared bloated, and commonly showed a difference in
172 mass between before and after the experiments.
173

Table 1. *Representative compositions for the starting glass, whole rock, clinopyroxene-hosted melt inclusions, and interstitial glass from the 1990, 2007, and 2014 eruptions.*

	Whole rock	Whole rock	Whole rock	Starting dry glass	Measured matrix glass[a]	Calculated matrix glass	Measured matrix glass	Cpx glass inclusions[a]	Cpx glass inclusions
Year	1990	2007	2014	1990	1990	2007	2014	1990	2014
n	1	1	1	10	27	1	5	15	5
Normalized wt. %									
SiO_2	54.3	54.9	55.3	55.0 (0.3)	68.4 (1.4)	69.3	67.1 (0.2)	69.1 (1.5)	68.5 (0.8)
TiO_2	0.7	0.6	0.6	0.6 (0.1)	0.53 (0.07)	0.9	0.6 (0.1)	0.5 (0.1)	0.7 (0.1)
Al_2O_3	19.0	18.6	18.5	19.0 (0.1)	15.4 (0.5)	14.0	15.5 (0.2)	16.0 (0.5)	15.7 (0.6)
FeO*	9.3	9.2	8.9	8.9 (0.5)	4.1 (0.3)	3.7	4.6 (0.2)	3.3 (0.9)	4.0 (0.3)
MnO	0.2	0.2	0.2	0.19 (0.04)	0.15 (0.02)	0.1	0.17 (0.05)	0.14 (0.04)	0.16 (0.05)
MgO	3.7	3.7	3.6	3.8 (0.1)	1.1 (0.1)	0.6	1.4 (0.1)	0.7 (0.4)	1.0 (0.1)
CaO	9.1	9.0	9.0	8.74 (0.09)	3.9 (0.4)	5.3	4.5 (0.1)	3.3 (0.6)	3.5 (0.3)
Na_2O	2.9	2.9	3.0	2.9 (0.1)	4.5 (0.2)	3.6	4.3 (0.2)	4.8 (0.5)	4.5 (0.3)
K_2O	0.7	0.7	0.7	0.68 (0.03)	1.6 (0.1)	2.1	1.6 (0.1)	1.8 (0.2)	1.63 (0.06)
P_2O_5	0.2	0.1	0.1	0.13 (0.02)	0.21 (0.03)	0.4	0.25 (0.03)	0.22 (0.04)	0.26 (0.04)
Original total	99.7	101.1	101.0	100.4 (0.9)	98.9 (1.0)	100.0	99.0 (0.3)	94.8 (1.3)	93.7 (0.7)
$Na_2O + K_2O$	3.6	3.6	3.7	3.6 (0.1)	6.0 (0.2)	5.7	5.9 (0.2)	6.5 (0.5)	5.7 (0.3)
Range of SO_3 (ppm)	n.a.	n.a.	n.a.	n.a.	57-138	n.a.	b.d.	395-1130	348-706
Cl (wt. %)	n.a.	n.a.	n.a.	0.030 (0.003)	0.12 (0.02)	n.a.	0.13 (0.01)	0.19 (0.01)	0.16 (0.02)

Note. n.a. = not analyzed. b.d.l. = below detection limit. [a]Average values of compositions from Chapter 1. Individual major element oxide compositions are normalized in wt. %, but original total is presented.

3.3 Experimental equipment

All experiments were conducted at Institut de Sciences de la Terre Orléans (France) using internally heated pressure vessel (IHPV), following the procedure outlined in Scaillet and Evans (1999). Argon was used as a pressurizing medium mixed with different H_2 concentrations at room temperature to establish different fO_2 conditions (ranging from NNO to NNO + 2), and using a Shaw membrane to establish and maintain the fH_2 osmotic equilibrium (Scaillet et al., 1992). A factory calibrated pressure transducer was used to measure and monitor pressure (± 2

MPa), whereas temperature was monitored with unsheathed type-S thermocouples, and the temperature of the hotspot was maintained at < 10°C and with an uncertainty of ± 5°C (Scaillet et al., 1992). Experiments were raised up to run temperature directly from room temperature in around an hour, where in each experimental run contained around 4-7 capsules, including one sensor for fO_2 (see below). Once the target run conditions were achieved, experiments were run for 18-66 hours. Experiments were terminated with a drop quench device, allowing the sample holder to fall in the cold part of the vessel at the bottom (< 50°C) ensuring isobaric quenching and cooling rates of 100°C/s. A fast quench device was set up as part of the experiments (Roux & Lefèvre, 1992). Previous studies have shown that crystal-melt equilibrium is attained using the same protocols. General observations of equilibrium include homogeneous glass composition within a given charge, lack of chemical zoning in experimental crystals, and systematic changes in petrologic variables (e.g. crystal content) with experimental variables (temperature and water content). Equilibrium, rather than quench, textures are characteristic of the run products we report and we believe they reflect attainment of chemical equilibrium at the desired run conditions.

3.4 Calculation of fO_2 and dissolved water content in experimental charges

The oxygen fugacity (fO_2) was calculated using a sensor capsule comprising two water-saturated (10mg added water), hand-pressed Ni-Pd-NiO powder pellets separated by inert ZrO powder (Taylor et al., 1992). We forgot to add a the sensor capsule for one experimental run (T = 1060°C, P = 200 MPa), and thus the final calculated fO_2 for the fluid saturated charge (XH_2O_{in} = 1.0) as the result of the average between the two closest isobaric runs (T = 1060°C, P = 100 and 400 MPa). For undersaturated charges, we calculated the fO_2 according to the following formula employed by Scaillet and Evans (1999):

$$fO_2\,(charge) = fO_2(sensor) + 2\left[log(H_2O)_{fluid}\,(charge)_{final}\right] \quad (1)$$

Where fO_2(charge) is the calculated oxygen fugacity of the charge, fO_2(sensor) is the sensor oxygen fugacity, and the $H_2O_{fluid}(charge)_{final}$ is the dissolved water content in the glasses. We could not calculate fO_2 for dry charges (no water in the melt). Finally, the water content of the experimental glasses was obtained by calculating the fluid composition through mass-balance

along with the solubility model for mixed H_2O-CO_2 fluids from Shishkina et al. (2010), with a relative error of ± 12 %.

3.5 Analytical techniques

Whole-rock analyses of samples, including the starting material pumice, were ground and fused into a lithium tetraborate disk before being analyzed for whole rock major element oxide compositions using X-Ray Fluorescence (XRF) at the Activation Laboratory in Ancaster, Canada following the approach outlined in Norrish and Hutton (1969). Mineral proportions were obtained by counting the phenocryst content using the JMicrovision software on plain polarized images of the entire thin section (for the 1990 samples), and using a Pelcon mechanical point counting stage (for the 2007 and 2014 samples). For each sample, we counted to 1400-1600 points to ensure statistically significant results with relative errors of < 10%. Results from point counting and mineral analyses (see below) allowed us to calculate the matrix glass of the 2007 dome samples through mass balance. Such calculations are necessary to remove the effect of the extensive microlite crystallization of the 2007 matrix, and we use such compositions for geothermobarometric calculations.

We made general observations of experimental charges, and identified phases using the scanning electron microscope (SEM) at ISTO-Orléans, France and the Earth Observatory of Singapore. We determined the crystal content of the experimental charges by thresholding the greyscale of multiple back-scattered electron (BSE) images of a charge map using ImageJ, we estimated the volumetric area of phases in all charges. From these results, we calculated the mass proportions of the main minerals using standard mineral densities.

Minerals and glass from natural samples and experimental charges were analyzed for their chemical compositions on the JEOL JXA-8530F electron microprobe (EPMA) at the Facility for the Analyses Characterization, Testing and Simulation (FACTS), Nanyang Technological University, Singapore. Analyses of orthopyroxene, clinopyroxene, olivine and Fe-Ti oxides were done on the EPMA in spot mode with 15 kV accelerating voltage, beam size of 1 μm, and 20nA beam current. Amphibole and plagioclase were analyzed in spot mode with 15 kV

accelerating voltage, beam size of 1 μm, and 10nA current. Glass was analyzed in spot mode with 6 kV, and beam size of 10 μm and 5 nA current. The same conditions and procedures were used to observe and analyze the glasses and minerals of the 2007 and 2014 rocks. For clinopyroxene-hosted glass inclusions, we corrected for post-entrapment crystallization of the melt inclusion walls (Bucholz et al., 2013). The relative errors for glasses are 0.4-0.8 % for SiO_2, Al_2O_3, and CaO; 1-3 % for MgO, FeO, Na_2O, K_2O; and 9-41% MnO, TiO_2, P_2O_5, and Cl. For pyroxenes, the relative errors are 0.2-1.0 % for SiO_2, Al_2O_3, and CaO, MgO, FeO; 1-30% for Na_2O, K_2O, and 2-55% MnO, TiO_2, and Cr_2O_3. Relative errors for Fe-Ti oxide analyses are 0.3-0.6% for FeO, 0.5-7.5% for TiO_2, 0.5-1.8% for MgO. For olivine analyses are 0.2-0.5% SiO_2, MgO, FeO; and 0.8-18% Al_2O_3, CaO, MnO. The relative error for the only amphibole analyses are 0.3-0.8% for SiO_2, Al_2O_3, CaO, FeO, MgO; 4.2-4.4% MnO, TiO_2; and 11-30% for Na_2O and K_2O.

The mineral end-members were calculated using their molar compositions as in Utami et al. (in revision) and according to Deer et al. (1992). Pyroxenes are characterized with the Mg # (Mg # = 100 × Mg / [Mg + Fe*] in mol, where Fe* is total iron as Fe^{2+}). We further characterize pyroxenes using their wollastonite (Wo = 100 × Ca / [Ca + Mg + Fe*]), ferrosilite (Fs = 100 × Fe / [Ca + Mg + Fe*]), and enstatite (En = 100 × Mg / [Ca + Mg + Fe*]) endmembers. Plagioclase end member compositions were classified using their molar compositions for anorthite (An = 100 × Ca / [Ca + Na + K]), albite (Ab = 100 × Na / [Ca + Na + K]), and orthoclase (Or = 100 × K / [Ca + Na + K]). Olivine is characterized using the forsterite content (Fo = 100 × Mg / [Mg + Fe*]), whereas amphibole is classified according to the compositional end-members outlined in Leake et al. (1997), as determined by Ridolfi et al. (2010). Glass compositions were characterized using their normalized to 100% anhydrous major element oxides and total alkali-silica (TAS) composition. It was difficult to obtain good quantitative analyses of plagioclase crystals in experimental charges as they are typically small and may contain Fe-Ti oxide inclusions. To be able to report approximate An contents of plagioclase, we have filtered for analyses with FeO* < 1 wt. % and TiO_2 < 0.1 wt. %, and subtracted the composition of magnetite from the electron microprobe analyses to match these constraints. We report these recalculated compositions to fit the structural formulae.

4 Results

4.1 Petrological observations and geothermobarometry of the 1990, 2007 and 2014 magmas

We made new petrological observations and geothermobarometric estimates from the deposits of the 1990, 2007, and 2014 eruptions (Tables 1-4). Whole rock major elements vary over a small range across eruptions and are classified as basaltic andesite (Table 1). The calculated matrix compositions, the measured interstitial glasses, and clinopyroxene-hosted melt inclusions are of a similar dacitic composition. The three eruptions have deposits with different phenocryst (> 100 μm) content: 31-47 wt. % in the 1990 pumices; 70-72 wt. % for the 2007 dome; and 29-35 wt. % in 2014 pumices (Table 2). The mineral assemblage for all three eruptions includes phenocrysts of plagioclase (Plag), clinopyroxene (Cpx), orthopyroxene (Opx), and magnetite (Mag). The 1990 and 2014 pumices also host partially reacted amphibole (Amph), and we have also identified pseudomorphs of Amph megacrysts and symplectites after Ol breakdown in the 2007 dome, meaning that both Amph and Ol may have also been stable in the 2007 magma. We also found partially reacted olivine (Ol) microphenocrysts (< 100 μm) in the 2014 pumice.

Table 2: *Mineral assemblage and phenocryst content of samples from 1990, 2007, and 2014 eruptions.*

Sample ID	90-23	PL1	2007A	2007B	14-PUMI-1	14-PUMI-2
Eruption	1990	1990	2007	2007	2014	2014
Phase[b]	wt. %	wt. %	wt. %	wt. %	wt. %	wt. %
Glm*	51.0	64.5	27.8*	30.2*	70.5	65.1
Plag	36.1	13.1	48.2	47.7	21.2	19.9
Cpx	4.5	6.0	4.6	3.9	1.2	2.1
Opx	4.1	7.9	10.6	12.0	3.0	7.5
Mag	4.3	8.4	8.5	6.2	3.6	4.7
Amph		0.1	0.3		0.5	
Ol						0.7
Total	100.0	100.0	100.0	100.0	100.0	100.0
Phenocryst content	49	35	72	70	29	34

295 *Notes.* [a]*For these samples Glm means matrix and include glass and microlites.* [b]*Opx =*
296 *orthopyroxene; Cpx = clinopyroxene; Plag = plagioclase; Mag = magnetite; Ol = olivine;*
297 *Amph = amphibole.*
298
299 Accessory minerals include ubiquitous apatite (Apa), which is found in all three
300 eruptions; quartz (Qz) rich enclaves occur in the 1990 late-stage pumice; and cristobalite (Crs) is
301 found as vesicle infill in the 2007 dome samples (See Supplementary Material). Ilmenite (Ilm) is
302 present as rims around Mag in the 1990 late-stage pumice, and as exsolution lamellae in Mag in
303 the 2007 deposits (See Supplementary Material). The compositions of the main minerals of the
304 three eruptions are also broadly similar, with the histograms of compositional mineral indicators
305 (e.g. Mg #) that typically overlap for the three eruptions (Fig. 1a-c; Table 3), and are also similar
306 to those of previous studies from the same eruptions (Cassidy et al., 2016, e.g. 2019; Jeffery et
307 al., 2013).
308
309

310
311 **Table 3**: *Summary of representative mineral compositions from the 1990-2014 eruption deposits.*
312

Mineral	Cpx	Cpx	Cpx	Opx	Opx	Opx	Mineral	Amph[a]	Amph
Eruption year	1990	2007	2014	1990	2007	2014	Eruption year	1990	2014
rock type/stage	main-stage pumice	dome	pumice	main-stage pumice	dome	pumice	rock type/stage		
Texture	cores, glom	cores, glom	cores, glom	cores, glom	glom	cores, glom	Texture		
n	8	16	17	11	7	9	n	18	4
wt. %									
SiO_2	51.6 (0.7)	51.8 (0.4)	51.1 (0.6)	52.8 (0.2)	52.9 (0.1)	52.6 (0.3)	SiO_2	41.6 (0.6)	43.0 (2.7)
TiO_2	0.5 (0.3)	0.33 (0.04)	0.4 (0.1)	0.19 (0.03)	0.16 (0.01)	0.19 (0.02)	TiO_2	1.5 (0.1)	1.7 (0.7)
Al_2O_3	1.8 (0.6)	1.7 (0.1)	2.2 (0.8)	1.0 (0.2)	0.9 (0.2)	1.0 (0.2)	Al_2O_3	14.9 (0.7)	11.9 (3.4)
FeO*	9.2 (0.6)	9.5 (0.1)	9.5 (0.4)	19.5 (0.3)	19.2 (0.2)	19.4 (0.3)	Cr_2O_3	0.05 (0.03)	
MnO	0.5 (0.1)	0.51 (0.03)	0.5 (0.1)	1.0 (0.2)	0.90 (0.04)	0.91 (0.04)	FeO*	11.3 (0.3)	10.5 (1.8)
MgO	14.5 (0.1)	14.3 (0.2)	14.5 (0.1)	23.1 (0.2)	22.84 (0.07)	23.1 (0.2)	MnO	0.15 (0.01)	0.13 (0.07)
CaO	21.1 (0.4)	20.8 (0.3)	20.6 (0.4)	1.4 (0.2)	1.44 (0.08)	1.45 (0.03)	MgO	13.9 (0.3)	14.7 (0.1)
Na_2O	0.27 (0.02)	0.29 (0.02)	0.3 (0.1)	0.01 (0.01)	0.02 (0.01)	0.015 (0.003)	CaO	12.0 (0.2)	12.0 (0.6)
K_2O							Na_2O	2.24 (0.8)	2.1 (0.4)
Total	99.4 (0.2)	99.3 (0.4)	99.0 (0.3)	99.0 (0.3)	98.4 (0.1)	98.7 (0.4)	K_2O	0.31 (0.02)	0.4 (0.02)
							Cl	0.016 (0.005)	
							F	0.13 (0.07)	
							Total	97.9 (0.4)	96.6 (0.2)
Pyroxene end-members[b]									
Wo	43.6 (0.8)	43.2 (0.6)	42.0 (0.6)	2.9 (0.4)	3.0 (0.2)	3.1 (0.1)	Amph end-member[d]	Mg-Hst	Ts-Prg
En	41.6 (0.3)	41.3 (0.5)	43.2 (0.8)	65.9 (0.3)	65.9 (0.3)	63.7 (0.4)			
Fs	14.9 (0.9)	15.5 (0.3)	14.8 (0.6)	31.2 (0.5)	31.1 (0.2)	33.2 (0.5)			
Mg #	73.6 (1.3)	72.8 (0.5)	73.9 (0.9)	67.8 (0.5)	67.9 (0.2)	65.7 (0.5)			

Mineral	Ol	Ol	Mineral	Plag	Plag	Plag	Plag
Eruption year	2014	2014	Eruption year	1990	2007	2014	2014
rock type/stage			rock type/stage	main-stage pumice	dome	pumice	pumice
Texture	low-Fo	high-Fo	Texture	microlite/rim	rim	core	rim
n	9	3	n	13	28	3	2
SiO_2	36.8 (0.2)	37.55 (0.33)	SiO_2	49.1 (1.2)	50 (2)	44.6 (0.1)	51.0 (0.1)
TiO_2	0.03 (0.02)	0.02 (0.02)	TiO_2		0.03 (0.03)	0.02 (0.02)	0.02 (0.01)
Al_2O_3	0.01 (0.02)	0.03 (0.03)	Al_2O_3	31.5 (1.0)	31 (1)	33.4 (0.2)	29.3 (0.1)
FeO*	26.6 (1.1)	23.41 (1.41)	FeO*	0.32 (0.05)	0.63 (0.06)	0.55 (0.02)	0.67 (0.01)
MnO	0.68 (0.05)	0.52 (0.07)	MnO		0.01 (0.01)		
MgO	34.5 (0.99)	37.06 (0.87)	MgO	0.04 (0.02)	0.05 (0.02)	0.06 (0.02)	0.08 (0.01)
CaO	0.17 (0.04)	0.2 (0.05)	CaO	14.8 (1.0)	14 (1)	18.4 (0.2)	13.42 (0.05)
Na_2O			Na_2O	3.4 (0.6)	3.5 (0.7)	1.2 (0.1)	3.9 (0.1)
K_2O			K_2O	0.06 (0.02)	0.09 (0.04)		
			Total	99.1 (0.5)	98.9 (0.5)	98.3 (0.2)	98.35 (0.01)
P_2O_5	0.04 (0.02)	0.03 (0.03)					
Total	98.9 (0.31)	98.8 (0.51)					
			Plag end-member[c]				
Fo content[e]	69.8 (1.5)	73.8 (1.6)	An	70.7 (5.3)	68 (7)	89.2 (0.9)	65.8 (0.5)
			Ab	29.0 (5.2)	31 (6)	10.8 (0.9)	34.2 (0.5)
			Or	0.3 (0.1)	0.6 (0.3)	n.a.	n.a.

Notes. n.a. = not analyzed. FeO or Fe* = total Fe as Fe^{2+}. Glom = glomerocryst. See Table 2 for meaning of mineral abbreviations.*

[a]Average amphibole composition From Utami et al. (in revision). [b]Pyroxene end-members: wollastonite, Wo = 100 x Ca / [Mg + Fe + Ca]; enstatite, En = 100 x Mg / [Mg + Fe* + Ca]; ferrosilite, Fs = 100 x Fe* / [Mg + Fe* + Ca]; Mg # = 100 x Mg / [Mg + Fe*].*

[c]Plagioclase end-members: anorthite, An = 100 x Ca / [Ca + Na + K]; albite, Ab = 100 x Na / [Ca + Na + K]; orthoclase, Or = 100 x K /[Na + Ca + K]. [d]Amphibole end-members according to Leake et al. (1997) as calculated in Ridolfi et al. (2010). Mg-Hst = magnesio-hastingsite; Ts-Prg = Tschermakite-Pargasite. [e]Olivine Fo content, Fo = 100 x Mg / [Mg + Fe].*

We made geothermobarometric estimates for the 1990-2014 magma storage and ascent conditions from mineral and glass/whole rock/matrix compositions (Table 4). For this we used core-whole rock and rim-interstitial/matrix glass pairs (see also Utami et al. (in revision) for the 1990 eruption). The pyroxene-liquid or two pyroxene equilibria formulations of Putirka (2008) give temperatures that range from about 1030°C for the crystal cores, to about 975°C (down to 950°C) for the crystal rims. Moreover, the mineral and glass compositions of the three eruptions give pre-eruptive temperatures that are within about ± 30°C (Table 4). These temperature estimates also overlaps with those obtained from amphibole-melt equilibria at about 960°C for the 1990 and 2014 eruptions. Pressure estimates we obtained come from the amphibole-melt geobarometer formulation of Putirka (2016), where pressures range from 450 MPa up to 700 MPa for the 1990 and 2014 eruptions, respectively.

Table 4. *Petrological storage conditions estimates from mineral-melt geothermobarometers, hygrometers and H_2O-CO_2 saturation models for the 1990, 2007, and 2014 mineral populations.*

Year	1990[a]				2007		2014			
Crystal Zone	core		rim		Core[f]		core		rim	
	n	T (°C)	n	T (°C)	n	T (°C)	n	T (°C)	n	T (°C)
Opx-melt[b]	75	1023 (19)	37	976 (17)	2	1032 (2)	15	1039 (15)	1	974
Cpx-melt[b]	122	1043 (13)	23	1045 (34)	5	1029 (3)	18	1028 (6)		
Two-px[b,c]	67	1023 (40)	67	1030 (43)	2	980 (9)			7	948 (8)
Ol-melt[b]							8	1018 (5)		

Year	1990				2007			2014			
	type	n	H_2O_{melt} (wt. %)	P_{sat} (MPa)[e]	zone	n	H_2O_{melt} (wt. %)	P_{sat} (MPa)[f]		n	H_2O_{melt} (wt. %)	P_{sat} (MPa)[g]
Plag-melt[d]	rim	9	4.1 (0.2)	172 (1)	core	82	4.4 (0.2)	189	core	2	6.0 (0.2)	214
	micr	9	4.1 (0.2)	170 (2)	rim	28	4.4 (0.2)	189	rim	2	4.0 (0.2)	168

Year	1990			2007			2014		
	n	T (°C)	P_{store} (MPa)	n	T (°C)	P_{store} (MPa)	n	T (°C)	P_{store} (MPa)
Amph-melt[h]	20	960 (10)	450 (80)	not analyzed			8	940 (80)	700 (90)

Note. Temperatures from pyroxene-based geothermometers were calculated using Putirka (2008) (SEE for Opx-liquid = ± 39°C; Cpx-liquid = ± 42°C; two-pyroxene = ± 60°C) and

Andersen et al. (1993) (± 37°C), assuming a constant pressure of 100 MPa. Temperatures from amphibole-melt geothermometer were calculated using Putirka (2016) (SEE = ± 30°C), with the Al/Si equilibrium test described in Li et al. (2021) ($^{Al/Si}K_d$ = 0.96 ± 0.4). Dissolved water content of main-stage pumices were calculated using the plagioclase-melt hygrometer of Waters and Lange (2015) (± 0.35 wt. %), and the saturation pressures were calculated using the Ghiorso and Gualda (2015) mixed H_2O-CO_2 saturation model. The saturation pressure and water content calculated for 2014 pumices were calculated in the same way as the 1990 eruption, but with the average estimated using the temperature calculated from two-pyroxene geothermometer of Putirka (2008) (SEE ± 37°C). Temperatures from the olivine-melt geothermometer were calculated using equation 21 of Putirka (2008) (SEE ± 36°C). See Table 2 for meaning of abbreviations; px = pyroxene; micr = microlite. Parameters in italics are average calculated values from Utami et al. (in revision) and this study. Numbers in parentheses refer to 1 standard deviation (sigma), but where the 1 sigma is lower than the error, the error is reported instead. [a]*The storage temperatures and pressures, water content and saturation pressures of the 1990 pumices were calculated in Utami et al. (in revision) using temperatures estimated from orthopyroxene rims and interstitial glass pairs.* [b]*Ol-melt geothermometer (Eq. 21); Opx-melt geothermometer (Eq. 28a); Cpx-melt geothermometer (Eq. 33); two-pyroxene geothermometer (Eq. 37) from Putirka (2008).* [c]*QUILF two-pyroxene geothermometer (Andersen et al., 1993).* [d]*Plag-melt hygrometer from Waters and Lange (2015) with minimum temperature estimates from Opx-melt and two-pyroxene geothermometers from Putirka (2008).* [e]*Saturation pressure and dissolved water contents for the 1990 eruption were estimated using Plag rims and microlites from Utami et al. (in revision) and the average Opx-melt temperature of 943 ± 48°C.* [f]*For 2007 dome samples, the calculated interstitial melt was used for rim Opx-liquid geothermometer calculations and Plag-melt hygrometer.* [g]*Saturation pressure is calculated with the MagmaSat application using a mixed H_2O-CO_2 model (Ghiorso and Gualda, 2015), and the average water content value from with the Plag-melt hygrometer.* [h]*Eq 7a (pressure) from Amph-melt geothermobarometer (Putirka, 2016) with Al/Si equilibrium K_d constant proposed in Li et al. (2020).*

The water content in the melt for the 1990 and 2014 magmas was calculated using the plagioclase-melt hygrometer of Waters and Lange (2015) using rim-interstitial glass pairs range

368 from 3 to 4 wt. % for an averaged temperature of T = 975°C, which is consistent with previous
369 estimates in Utami et al. (in revision). These water contents in the melt correspond to water
370 saturation pressures of 170-190 MPa, which also is similar to the range of pressures obtained in
371 Utami et al. (in revision). Surprisingly, the water content in the melt estimated for the 2007
372 samples using plagioclase rim and core and the calculated matrix glass is ~4 wt. % water, and
373 thus similar to those of the 1990 and 2014 eruptions.
374 Another important aspect to consider towards improving our understanding the volatile
375 content of these eruptions is the likely existence of an exsolved fluid phase at pre-eruptive
376 eruptions. Utami et al. (in revision) calculated the amount of S that could be degassed for the
377 1990 eruption and estimated that 0.01-0.12 Mt could reside in an excess volatile phase. We have
378 done the same calculation of the sulfur budget for the 2014 magma and satellite measurements;
379 (see Methodology section), and we find a range of excess volatile phase of 0.08-0.10 Mt of S
380 (Table 11).
381

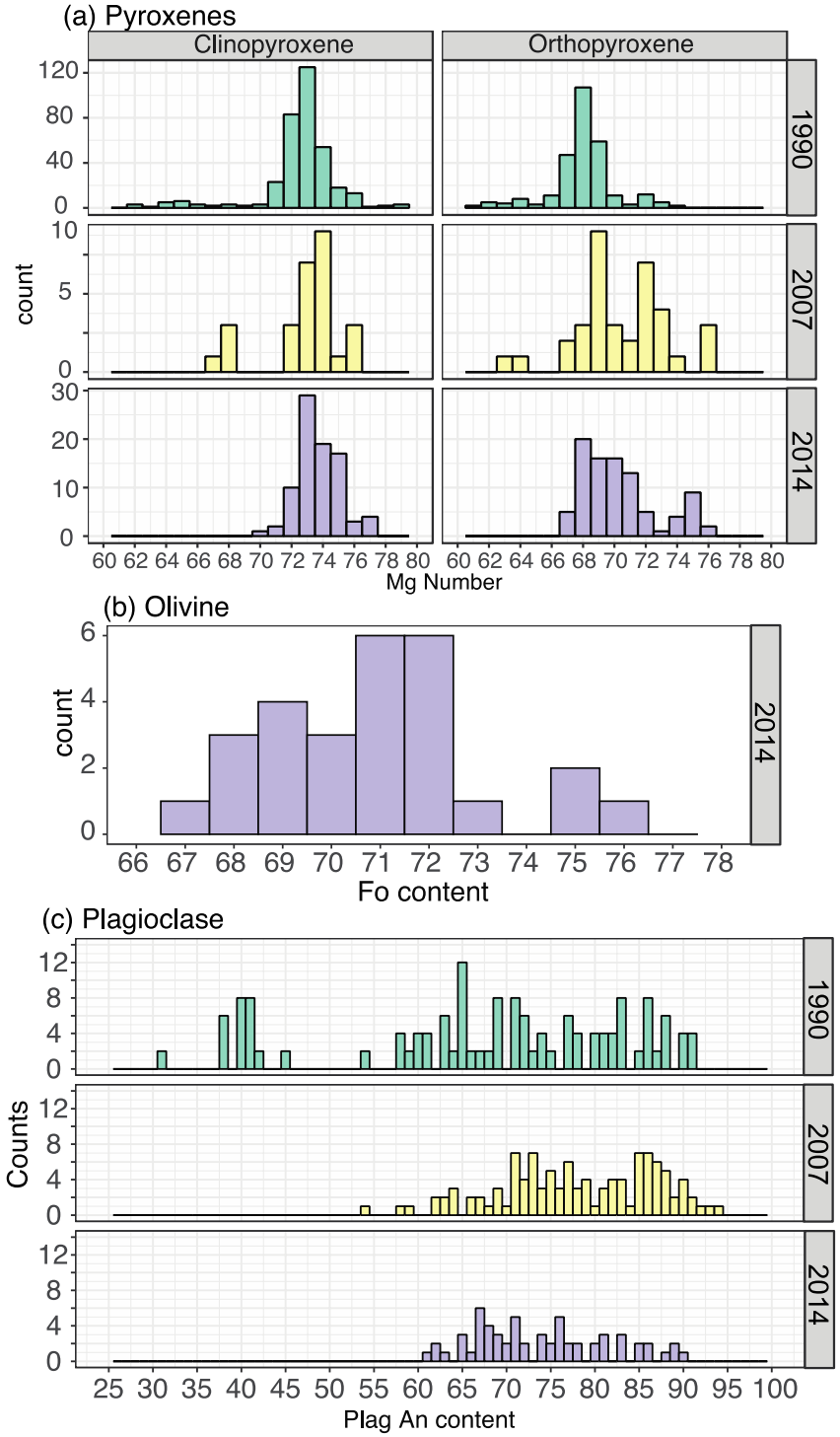

382 ***Figure 1.*** *Histograms of representative mineral compositions from the 1990-2014 eruptions:* ***a.***
383 *pyroxenes,* ***b.*** *olivine, and* ***c.*** *plagioclase. Plagioclase composition from the 2014 eruption comes*
384 *from a combination of this study and Cassidy et al. (2016) and those of the 1990 from Utami et*
385 *al. (in revision).*

386

387 4.2 General observations from the experimental results

388 Successful experimental charges range from complete glass to almost fully crystallized.
389 Glass-rich charges are devoid of vesicles (Fig. 2). Most charges (Fig. 2b-e, g-h) have a
390 porphyritic texture, with subhedral to euhedral crystals set in interstitial glass with vesicles.
391 Crystals may vary in size from phenocrysts (> 100 μm) to microlites (< 10 μm). Typically, Opx
392 and Ol are subhedral to euhedral, commonly with Mag and Plag inclusions (>100 μm) (Fig. 2c).
393 Some charges have clusters of Fe-Ti oxides microlites, as well as Fe-Ti oxides distributed
394 throughout the charge (Fig. 2d). Despite the large range in crystal sizes, minerals and glass
395 appears to be unzoned, according to BSE images, which is likely indicative of compositional
396 equilibrium. Due to the small size of many crystals, it was very challenging to obtain a good
397 quantitative chemical analysis, and thus we relied on mineral identification using EDS spectra
398 obtained in SEM or electron probe. We obtained glass compositions from glass-rich
399 experimental charges or for those where glass "pools" larger than about 10 μm, and we found
400 that they are homogeneous in composition (Fig. 2a-d). For charges with low water contents,
401 phases are often too small to analyze. For charges that failed i.e. where the fluid escaped the
402 capsule during the experiment, we consistently observe a very high crystal content and a quench
403 texture, with abundant microlites of Opx and Plag, and rare Ilm and glass; these were not used
404 further.
405

406 4.3 Phase relation, crystallinities, and mineral assemblages

407 The full experimental phase assemblage of all charges includes Opx ± Cpx ± Plag ± Mag
408 ± Ilm ± Amph ± Ol + glass (Fig. 2a-h). We did not identify experimental apatite, but we cannot
409 rule out that it is not present. The crystal content from experimental charges varies from virtually
410 none to about 88 wt. % (Table 5), and increases as temperature and water content decreases, and
411 also as fO_2 also increases. We produced liquidus or near- liquidus experiments with < 1 wt. % of
412 crystals at 1060°C, NNO at water saturated conditions (about 5-9 wt. % H_2O in the melt) and at
413 200 and 400 MPa (Fig. 2a). These conditions match with the model liquidus temperature
414 calculated from rhyolite-MELTS in Utami et al. (in revision). At 100 and 200 MPa and 1000°C,

415 the crystal content is varies between about 68 to 44 wt. % for 2-4 wt. % water in the melt.
416 Increasing the temperature to 1060°C decreases the crystal content to 52 to 31 wt. % at 3-4 wt. %
417 water in the melt, but it increases up to 74 wt. % for < 2 wt. % in the melt. Similar changes in
418 crystal content with temperature and water content in the melt for different experimental
419 pressures. The effect of increasing fO_2 from NNO to NNO + 2 is to increase somewhat the
420 proportion of magnetite with comparable crystal content.
421

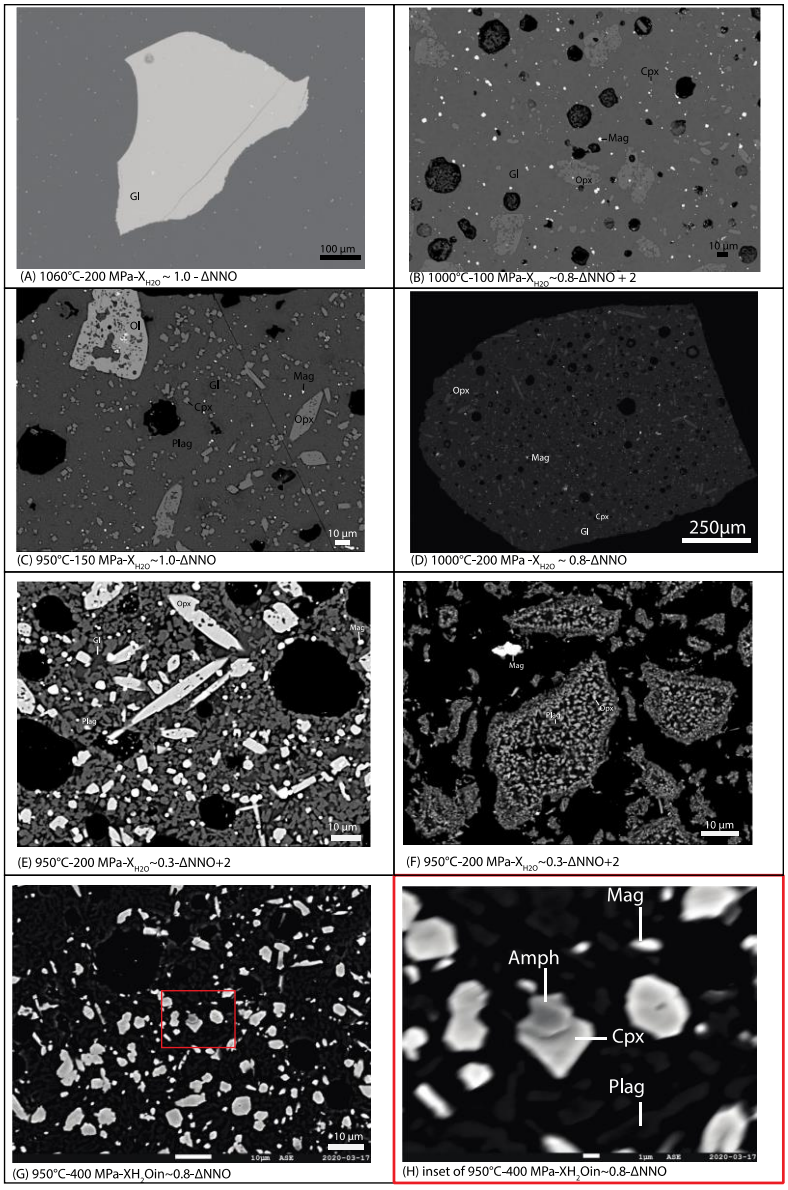

422

Figure 2 *Annotated BSE images of selected representative experimental charges in order of decreasing crystallinity.* ***a.*** *1060°C-200 MPa-NNO.* ***b.*** *1000°C-100 MPa-NNO + 2.* ***c.*** *950°C-150 MPa-NNO.* ***d.*** *1000°C-200 MPa-NNO.* ***e.*** *950°C-200 MPa-ΔNNO + 2.* ***f.*** *950°C-200 MPa-NNO + 2.* ***g.*** *950°C-400 MPa-NNO.* ***h.*** *Inset of charge in* ***g.*** *labelled with abbreviated mineral names (Gl = glass, Plag = plagioclase, Cpx = clinopyroxene, Opx = orthopyroxene, Mag = magnetite, Amph = amphibole).*

The relationship between crystallinity, temperature, and water content in the melt can be used to obtain first order constraints on the pre-eruptive conditions (Fig. 3). Using a pre-eruptive temperature storage of about 975 ± 39°C for the three eruptions, as suggested by geothermobarometric data of all eruptions (Table 4), we find that the 1990 and 2014 melt coul contain about 4-6 wt. % water, or 4-5 wt. % at 100-200 MPa. The much higher phenocryst content of the 2007 dome would imply significantly lower water content in the melt (~1 wt. %). However, as we have discussed in the geothermobarometry results section above, we believe this does not reflect the pre-eruptive conditions, as the plagioclase-matrix equilibria suggest similar water contents in the melt for the 2007 and the 1990 and 2014 eruptions, and rather reflects re-equilibration and maturation during slow ascent, as further discussed below.

We find that experimental Opx and Plag are present at all conditions below the liquidus, and Cpx stability field has a somewhat smaller stability field (Fig 4a-c, Fig. S4 of Supplementary Material). We identified experimental amphibole at 950-1000°C and 200-400 MPa, with 4.5-6 wt. % water in the melt (Fig 4a-b). Despite our efforts we were not able to positively identify Amph at lower pressures (< 200 MPa) and 950°C charges owing to the high crystallinity and small crystal sizes, although we suspect it is stable by comparing to the results of other phase equilibria studies with similar bulk compositions (e.g. Erdmann et al., 2016; Pichavant et al., 2002; Prouteau & Scaillet, 2003). We identified experimental Ol with 3-4 wt. % water in the melt at NNO and < 150 MPa (Fig. 4b). At NNO + 2, Ol stability extends to higher pressures and water content (at 200 MPa, 1000°C, and 3-6 wt. % water in the melt; Fig 4c). The stability of Fe-Ti oxides is also controlled by the dissolved water content and fO_2. Ilmenite is stable at lower dissolved water contents than magnetite, whereas with increasing fO_2 makes magnetite more stable at low water contents. Given the wide stability field of pyroxenes and plagioclase, the

most diagnostic mineral to establish the pre-eruptive conditions is the presence of Amph in the 1990 and 2014, and xenocrysts and pseudomorphs in the 2007 lava domes. Amph stability requires water contents of ≥ 3 wt. % in the melt, T < 1000°C and P ≥ 200 MPa. Cassidy et al. (2019) conducted experiments using the 2014 Kelud rock, and the stability of anhydrous minerals they reported are quite similar to those we found, but did not explore the P-T-water content in the melt at which Amph is stable; thus they did not experimentally grow the mineral.

Table 5. *Summary of experimental results, including crystal content, mineral assemblage and normalized mineral proportions and original major element totals. Dissolved H_2O and CO_2 concentrations were calculated using the H_2O-CO_2 solubility model of Shiskina et al. (2010).*

				Calculated melt volatile content[d]			Phase proportions[e,f] (wt. %)								
Charge ID	$\log(fO_2)$[a] (bar)	ΔNNO[b]	XH_2O_{in}[c]	XH_2O_{fluid}	H_2O_{melt} (wt. %)	$CO_{2\text{-melt}}$ (wt. ppm)	Opx	Cpx	Plag	Mag	Ilm	Ol	Amph	Gl	Total
T = 1000°C, P = 100 MPa, t = 66 hours															
SUPL1-1	-9.5	0.8	1.00	1.0	3.5	0	6.0	2.8	30.4	1.1		3.4		56.3	100
SUPL1-2	-9.8	0.6	0.80	0.7	3.0	162	12.4	8.1	29.6	2.1				47.8	100
SUPL1-3	-10.3	0.1	0.66	0.6	2.5	267	13.2	8.7	33.9	2.7				41.5	100
SUPL1-4	-10.9	-0.6	0.56	0.5	2.3	312	14.9	8.3	42.8	2.3				31.7	100
T = 1000°C, P = 150 MPa, t = 19 hours															
SUPL1-5	-8.5	1.8	1.00	1.0	4.4	0	18	25	2					55.0	100
SUPL1-6	-8.7	1.6	0.82	0.8	3.8	250	3.7	2.3	23.3	0.5		4.3		65.9	100
SUPL1-7	-9.0	1.4	0.67	0.6	3.2	414	13.1	7.6	29.7	1.8				47.8	100
SUPL1-8	-9.0	1.3	0.63	0.6	3.1	444	13.4	12.1	34.6	1.8				38.1	100
SUPL1-9	-9.5	0.9	0.41	0.3	2.3	633	13.4	5.3	55.9	3.7				21.8	100
SUPL1-10	n.a.	n.a.	0.00	0.0	0.0	888	23.7		57.8		0.7			17.9	100
T = 1000°C, P = 200 MPa, t = 22 hours															
SUPL1-11	-9.1	1.2	1.00	-	-	-	-	-	-	-	-	-	-	-	-
SUPL1-12	-9.4	0.9	0.84	0.7	4.4	421	7.6	4.1	25.9	0.9				61.6	100
SUPL1-13	-9.6	0.8	0.75	0.6	3.9	573	5.1	6.8	29.2	1.0				57.9	100
SUPL1-14	-9.9	0.4	0.55	0.4	3.1	835	11.2	8.2	35.8	1.2				43.5	100
SUPL1-15	-10.7	-0.4	0.30	0.2	1.8	1090	14.6	15.3	36.0	0.6				33.5	100
SUPL1-16	n.a.	n.a.	0.00	0.0	0.0	1263	25.3		53.1		0.6			21	100
T = 1000°C, P = 400 MPa, t = 23 hours															
SUPL1-17	-9.2	1.1	1.00	1.0	8.3	-	-	-	-	-	-	-	-	-	-
SUPL1-18	-9.5	0.8	0.85	0.7	6.5	1681	13.9	1.8	5.6	0.3			< 0.01	78.4	100
SUPL1-19	-10.4	0.0	0.54	0.3	3.8	2977	16.5	12.0	21.6	0.3				49.6	100
SUPL1-20	-11.4	-1.0	0.27	0.1	1.9	3438	16.0	12.0	28.5	0.8				42.7	100
SUPL1-21	n.a.	n.a.	0.00	0.0	0.0	3638	25.0		37.7		0.4			36.9	100
T = 950°C, P = 150 MPa, t = 66 hours															

				Calculated melt volatile content[d]			Phase proportions[e,f] (wt. %)								
Charge ID	$\log(fO_2)$[a] (bar)	ΔNNO[b]	XH_2O_{in}[c]	XH_2O_{fluid}	H_2O_{melt} (wt. %)	$CO_{2\text{-melt}}$ (wt. ppm)	Opx	Cpx	Plag	Mag	Ilm	Ol	Amph	Gl	Total
SUPL1-22	-10.0	1.1	1.00	1.0	4.3	0	7.1	1.2	19.3	3.5		5.1		63.8	100
SUPL1-23	-10.2	0.9	0.84	0.8	3.7	245	14.4	3.6	29.3	4.3				48.4	100
SUPL1-24	-10.3	0.8	0.75	0.7	3.5	327	16.8	7.6	27.8	0.6				47.2	100
SUPL1-25	-10.8	0.3	0.49	0.4	2.5	582	14.0	10.8	33.8	0.8				40.6	100
SUPL1-26	-11.0	0.1	0.39	0.3	2.2	647	13.5	11.0	42.5	0.6				32.4	100
SUPL1-27	n.a.	n.a.	0.00	0.0	0.0	890	35.5		52		0.5			12	100
T = 950°C, P = 200 MPa, t = 49 hours															
SUPL1-28	-10.7	0.4	1.00	1.0	5.1	0	19.9	13.2	28.6	3.0				35.2	100
SUPL1-29	-10.9	0.2	0.86	0.8	4.6	291	19.0	7.6	38.5	4.3				30.7	100
SUPL1-30	-11.1	0.0	0.68	0.6	3.8	588	17.7	20.6	31.9	0.9				28.8	100
SUPL1-31	-11.4	-0.3	0.54	0.4	3.2	797	12.8	15.4	44.0	1.6				26.3	100
T = 950°C, P = 400 MPa, t = 67 hours															
SUPL1-32	-9.8	1.3	1.00	1.0	8.1	0	17.9	8.4	10.7	3.2				60.0	100
SUPL1-33	-10.3	0.8	0.78	0.6	5.8	2066	14.3	3.7	16.0	3.0			< 0.01	63.0	100
SUPL1-34	-10.6	0.6	0.71	0.4	4.9	2526	11.2	3.9	29.4	3.2				52.3	100
SUPL1-35	-11.0	0.1	0.50	0.3	4.3	3029	11.0	2.9	35.2	3.2				47.7	100
SUPL1-36	-11.5	-0.4	0.35	0.1	2.6	3322	12.9	10.2	30.5	2.7				43.6	100
SUPL1-37	n.a.	n.a.	0.00	0.0	0.0	3685	30.4		39.4		0.4			29.8	100

464 **Table 5.** Experimental conditions and run product information (continued).

				Calculated melt volatile content[d]			Phase proportions[e,f] (wt. %)								
Charge ID	$\log(fO_2)$[a] (bar)	ΔNNO[b]	XH_2O_{in}[c]	XH_2O_{fluid}	H_2O_{melt} (wt. %)	$CO_{2\text{-melt}}$ (wt. ppm)	Opx	Cpx	Plag	Mag	Ilm	Ol	Amph	Gl	Total
T = 1060°C, P = 100 MPa, t = 18 hours															
SUPL1-38	-8.1	1.4	1.00	1.0	3.6	0			28.7	1.9				69.3	100
SUPL1-39	-8.4	1.1	0.78	0.7	3.0	168			56.8	2.4		< 0.1		40.8	100
SUPL1-40	-8.8	0.7	0.73	0.6	2.8	220			46.0	3.6		0.9		49.5	100
SUPL1-41	-9.2	0.2	0.67	0.6	2.6	251	4.9	3.1	43.6	0.4				48.0	100
SUPL1-42	-10.3	-0.9	0.37	0.3	1.7	424	9.5	7.7	43.6	3.7				35.5	100
SUPL1-43	n.a.	n.a.	0.00	0.0	0.0	563	22.5	0.8	38.1		12.6			26.0	100
T = 1060°C, P = 200 MPa, t = 94 hours															
SUPL1-44	-8.4	1.1	1.00	1.0	5.3	0			0.8					99.2	100
SUPL1-45	-8.9	0.5	0.72	0.5	3.6	696	16.6	2.1	16.9	2.1				62.4	100
SUPL1-46	-9.3	0.1	0.53	0.3	2.8	914	12.9	7.9	28.2	0.9				50.1	100
SUPL1-47	-10.3	-0.8	0.27	0.1	1.4	1153	20.1	1.3	37.6	2.0				39.0	100
SUPL1-48	n.a.	n.a.	0.00	0.0	0.0	1260	21.5		42.6	0.9				35.0	100
T = 1060°C, P = 400 MPa, t = 49 hours															
SUPL1-49	-8.6	0.9	1.00	1.0	8.6	0								100.0	100
SUPL1-50	-10.1	-0.7	0.59	0.2	3.0	3206	2.7	1.8	13.8	0.2				81.5	100
SUPL1-51	-11.6	-2.1	0.22	0.0	1.1	3543	9.1	6.4	21.8	1.7				61.0	100
T = 1000°C, P = 100 MPa, t = 77 hours															
SUPL1-52	-8.4	1.9	1.00	1.0	3.5	0	5.8	5.6	25.8	3.2		0.9		58.7	100
SUPL1-53	-8.6	1.7	0.83	0.8	3.0	143	11.0	2.5	29.2	2.8				54.5	100
SUPL1-54	-8.7	1.6	0.77	0.7	2.9	178	11.8	4.3	30.6	2.8				50.5	100
SUPL1-55	-9.0	1.3	0.57	0.5	2.3	311	13.7	4.1	38.1	3.1				41.0	100
SUPL1-56	-9.4	0.9	0.42	0.3	1.8	399	16.0	11.1	33.2	0.4				39.3	100
SUPL1-57	n.a.	n.a.	0.00	0.0	0.0	564	23.9		44.7		2.4			29.0	100
T = 1000°C, P = 200 MPa, t = 19 hours															
SUPL1-58	-8.5	1.8	1.00	1.0	5.2	0	14.3	3.1	15.7	0.6				66.0	100
SUPL1-59	-8.7	1.6	0.85	0.8	4.5	355	2.0	1.5	20.2	1.0		4.0		71.2	100
SUPL1-60	-8.9	1.4	0.73	0.6	3.9	575	6.4	4.7	21.4	3.3		5.9		58.4	100
SUPL1-61	-9.1	1.2	0.59	0.5	3.5	726	13.2	6.3	28.3	1.6				50.6	100
SUPL1-62	-10.0	0.3	0.29	0.2	1.9	1086	15.5	13.0	28.0	3.0				40.6	100
SUPL1-63	n.a.	n.a.	0.00	0.0	0.0	1263	22.5		39.0		9.4			29.0	100
T = 950°C, P = 200 MPa, t = 71 hours															
SUPL1-64	-9.3	1.8	1.00	1.0	5.1	0	15.3	18.0	19.9	1.0				45.7	100
SUPL1-65	-9.5	1.7	0.86	0.8	4.5	303	16.7	5.2	31.4	3.7				43.0	100

				Calculated melt volatile content[d]			Phase proportions[e,f] (wt. %)								
Charge ID	$\log(fO_2)$[a] (bar)	ΔNNO[b]	XH_2O_{in}[c]	XH_2O_{fluid}	H_2O_{melt} (wt. %)	$CO_{2\text{-melt}}$ (wt. ppm)	Opx	Cpx	Plag	Mag	Ilm	Ol	Amph	Gl	Total
SUPL1-66	-9.7	1.4	0.73	0.6	3.8	583	-	-	-	-	-	-	-	-	-
SUPL1-67	-10.0	1.1	0.54	0.4	3.1	804	15.0	11.1	34.3	3.1				36.4	100
SUPL1-68	-10.9	0.2	0.28	0.2	1.7	1104	25.5	22.2	21.4	0.5				30.5	100
SUPL1-69	n.a.	n.a.	0.00	0.0	0.0	1266	42.6		41.4		0.6			15.4	100

Note. [a]*$\log(fO_2)$ determined using water saturated Ni-Pd alloy capsules, calculated using the formulation by Pownceby and O'Neill (1994). For undersaturated charges, we calculated the fO_2 using the formula outlined in section 3.4.* [b]*$\Delta NNO = \log(fO_2)$ - $\log(fO_2)$ at Ni-NiO buffer .* [c]*$XH_2Oin = H_2O/(H_2O + CO_2)$ loaded in capsules in moles.* [d]*Water and CO_2 content in the melt were calculated from mass balance combined with the mixed H_2O-CO_2 solubility model of Shishkina et al. (2010) for H_2O and Dixon et al. (2008) for CO_2.* [e]*Phase proportions were calculated using grayscale thresholding of BSE charge maps using ImageJ software and then converted to phase proportions.* [f]*See Table 2 for meaning of abbreviations, with the addition of Gl that we refer to glasses only. For charges where only CO_2 was added, we could not calculate the log (fO_2).*

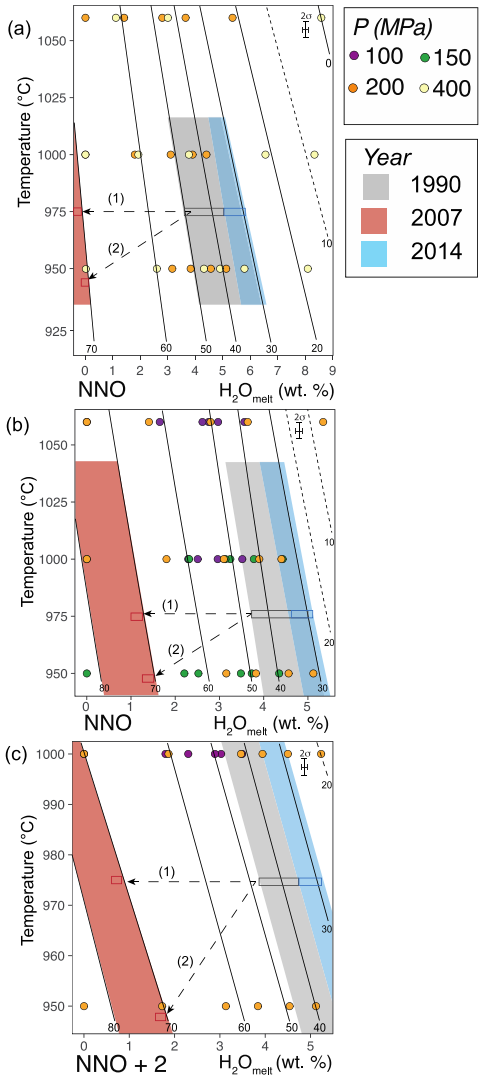

Figure 3. *Dissolved water content versus crystal content of experimental charges for* ***a.*** *200-400 MPa,* ***b.*** *100-200 MPa at NNO, and* ***c.*** *100-200 MPa at NNO + 2. Dashed lines denote extrapolated crystal contents of experimental charges. Grey, red and blue semi-transparent boxes represent the field bounded by the phenocryst content of natural samples, water content in the melt for the given temperature with SEE errors (975 ± 39°C) for the 1990 pumices (explosive), 2007 dome fragments (effusive), and 2014 pumices (explosive). Dashed arrows indicate possible changes of temperature and water in the melt during ascent for the 2007 magma. The crystal contents were obtained by Utami et al. (in revision) and this study (Table 1). Average temperature estimates from each eruption are calculated from mineral-melt geothermobarometry listed in Table 3.*

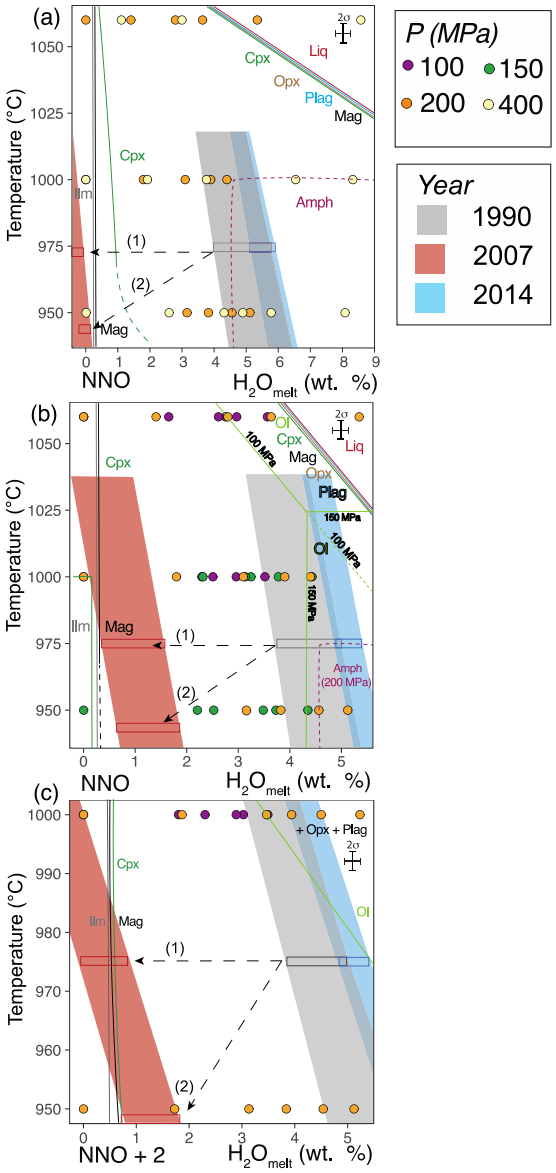

Figure 4 *Phase relations for* ***a.*** *200-400 MPa,* ***b.*** *100-200 MPa at NNO, and* ***c.*** *100-200 MPa at NNO + 2. Grey, red and blue semi-transparent boxes represent the same parameters as Fig. 3. Dashed lines denote inferred phase stability fields at the given temperature and water content. Dashed arrows indicate potential degassing pathways. The phenocryst contents were estimated from Utami et al. (in revision) and this study (Table 1). Mineral name abbreviations are the same as in Fig 1, with the addition of Liq for liquid and Ilm for ilmenite. Pressure specific stability are specified next to the boundary line. Red line with 'liq' represents the liquidus boundary at the given pressure and temperature.*

4.4 Mineral and glass compositions

4.4.1 Glass

Experimental glass compositions vary with water content and temperature (Fig 5a-h), with compositions ranging from basaltic andesite to dacite as temperature decrease from 1060 to 950°C (Table 6). The most evolved glass that we were able to analyze has 67 wt. % SiO_2 is at 200 MPa, 1060°C, NNO at 1 wt. % water, with 50-54 wt. % crystals in the charge (Fig. 5a). The glass we analyzed from the rest of the charges range from basaltic andesite to andesite. For the same temperature, pressure, and fO_2, oxides such as SiO_2, K_2O, and CaO increases as water content in the melt decreases, indicating the melt is becoming more evolved (Fig. 5a, c, e). Changing the fO_2 from NNO to NNO + 2 does not significantly affect the SiO_2 content of the melt for the same pressure, temperature, and dissolved water content. The FeO* (3.5-9 wt. %), MgO (0.6-3.9 wt. %), and CaO (5-9.5 wt. %) of experimental glasses (Fig 5d-f) are controlled by crystallization of ferromagnesian minerals such as pyroxenes and magnetite. The limited number of natural and experimental glasses that we were able to analyze preclude direct and detailed comparisons that would allow to establish the pre-eruptive conditions. The lack of agreement between the matrix glass compositions and experimental glasses could be due to the effect of syn-eruptive crystallization. These typically manifests as Plag microlites in natural rocks. We observe microlites in one 1990 pumice and the 2007 dome, which would explain why the natural rocks have a higher SiO_2 content than the experimental glasses.

Table 6. Experimental glass chemistry.

T (°C)	1000	1000	1000	1000	1000	1000	1000	1000	1000	1000	950
Charge[a]	SUPL 1-1	SUPL 1-2	SUPL1-6	SUPL1-7	SUPL1-8	SUPL1-12	SUPL1-13	SUPL1-16	SUPL1-17	SUPL1-19	SUPL1-21
n:	1	1	4	2	3	1	1	4	2	1	1
wt. %											
SiO_2	52.8	56.1	57.4 (0.6)	60.1 (0.6)	58 (2)	56.5	59.6	56.7 (0.7)	56.1 (0.7)	55.8	61.2
TiO_2	0.5	0.4	0.7 (0.1)	0.9 (0.2)	0.8 (0.2)	0.7	0.8	0.6 (0.1)	0.9 (0.3)	0.5	0.7
Al_2O_3	20.8	23.4	19 (2)	16.40 (0.01)	20 (3)	20.5	17.0	22 (1)	18.8 (0.7)	23.0	17.1
FeO*	6.3	4.7	6.9 (0.5)	8.3 (0.2)	7 (2)	7.4	8.6	6.3 (0.5)	9.2 (0.5)	5.2	7.8
MnO	0.1	0.1	0.17 (0.01)	0.20 (0.01)	0.17 (0.03)	0.2	0.2	0.13 (0.02)	0.18 (0.01)	0.1	0.3
MgO	1.9	1.6	2.8 (0.3)	2.7 (0.1)	2.0 (0.5)	2.1	2.2	1.4 (0.2)	3.1 (0.2)	1.2	2.3

CaO	9.0	9.7	8.6 (0.9)	6.69 (0.01)	8 (2)	8.7	6.5	8.7 (0.7)	7.6 (0.3)	9.6	6.3
Na_2O	3.0	3.3	3.2 (0.1)	3.1 (0.1)	3.37 (0.09)	3.0	3.7	3.4 (0.1)	3.2 (0.03)	3.5	3.1
K_2O	0.6	0.7	0.8 (0.1)	1.22 (0.01)	0.9 (0.2)	0.8	1.1	0.9 (0.1)	0.80 (0.04)	0.7	0.2
P_2O_5	0.1	0.2	0.17 (0.02)	0.27 (0.03)	0.19 (0.06)	0.1	0.2	0.17 (0.03)	0.17 (0.02)	0.2	1.1
Total[b]	95.0	96.2	89.8 (0.3)	87.2 (1.0)	90.2 (0.8)	95.3	94.0	95.2 (1.0)	91.9 (0.8)	93.7	85.8
TAS content	3.7	4.0	4.0	4.3	4.3	3.8	4.9	4.3	4.0	4.2	4.9
H_2O content[c]	3.5	3	3.8	3.2	3.1	4.4	3.9	8.3	6.5	3.8	4.3
T (°C)	1060	1060	1060	1060	1060	1060	1060	1060	1060	1060	1060
Charge[a]	SUPL 1-37	SUPL 1-38	SUPL1-39	SUPL1-40	SUPL1-41	SUPL1-43	SUPL1-44	SUPL1-45	SUPL1-46	SUPL1-48	SUPL1-49
n:	3	5	4	4	1	5	2	3	1	4	4
wt. %											
SiO_2	56.4 (0.04)	56.5 (0.6)	55.9 (0.9)	56.7 (0.4)	59.6	55.0 (0.6)	60 (2)	57.8 (0.3)	66.6	56.0 (0.4)	57.6 (0.2)
TiO_2	0.66 (0.06)	0.7 (0.1)	0.6 (0.1)	0.8 (0.1)	1.0	0.7 (0.1)	1.0 (0.1)	0.80 (0.03)	1.7	0.6 (0.1)	0.70 (0.02)
Al_2O_3	18.5 (0.3)	19 (2)	20 (2)	19 (2)	16.7	18.8 (0.1)	18 (3)	21.9 (0.1)	14.9	19.2 (0.03)	17.5 (0.1)
FeO*	7.4 (0.2)	6.7 (0.8)	5.9 (0.9)	6.2 (0.4)	7.1	8.5 (0.3)	8 (1)	4.6 (0.01)	3.5	7.4 (0.2)	7.5 (0.1)
MnO	0.22 (0.03)	0.21 (0.03)	0.20 (0.03)	0.19 (0.03)	0.3	0.2 (0.03)	0.2 (0.1)	0.12 (0.01)	0.1	0.2 (0.05)	0.22 (0.01)
MgO	4.2 (0.1)	3.88 (0.04)	3.6 (0.5)	3.5 (0.3)	3.4	4.0 (0.1)	1.6 (0.3)	0.68 (0.04)	2.0	3.8 (0.1)	4.1 (0.02)
CaO	8.6 (0.2)	8.9 (0.8)	9.5 (0.9)	9.4 (0.7)	7.7	9.03 (0.03)	7 (2)	9.1 (0.1)	5.4	9.1 (0.1)	8.2 (0.1)
Na_2O	3.1 (0.1)	3.1 (0.1)	3.1 (0.1)	3.0 (0.1)	3.0	3.0 (0.1)	3.6 (0.2)	3.6 (0.1)	3.7	2.8 (0.05)	3.1 (0.04)
K_2O	0.75 (0.02)	0.8 (0.1)	0.6 (0.1)	0.8 (0.1)	1.0	0.69 (0.01)	1.2 (0.2)	1.00 (0.02)	1.9	0.6 (0.04)	0.8 (0.01)
P_2O_5	0.15 (0.02)	0.15 (0.01)	0.14 (0.04)	0.14 (0.03)	0.2	0.13 (0.01)	0.2 (0.1)	0.21 (0.03)	0.3	0.1 (0.02)	0.2 (0.01)
Total[2]	92.6 (0.2)	94 (1)	93.7 (0.06)	93 (1)	93.6	92.3 (0.6)	95.1 (0.3)	96.7 (0.3)	94.8	90.5 (0.4)	94.9 (0.4)
TAS content	3.8	3.8	3.7	3.8	4.0	3.7	4.9	4.6	5.6	3.4	3.9
H_2O content[3]	3.6	3.0	2.8	2.6	1.7	5.3	3.6	2.8	1.4	8.6	3.0
T (°C)	1000	1000	1000	1000	1000	1000	1000				
Charge[a]	SUPL 1-52	SUPL 1-53	SUPL1-54	SUPL1-55	SUPL1-58	SUPL1-59	SUPL1-60				
n:	1	1	2	1	5	1	3				
wt. %											
SiO_2	54.8	56.2	56.0 (0.4)	59.6	56.7 (0.2)	57.8	59.5 (0.09)				
TiO_2	0.3	0.5	0.70 (0.02)	0.6	0.68 (0.05)	16.8	1.0 (0.04)				
Al_2O_3	25.5	22.1	21.8 (0.1)	18.9	18.3 (0.6)	7.3	15.99 (0.09)				
FeO*	3.2	5.7	5.8 (0.4)	6.6	8.1 (0.2)	3.2	9.1 (0.2)				
MnO	0.1	0.1	0.14 (0.02)	0.2	0.20 (0.02)	3.2	0.23 (0.01)				

MgO	1.0	1.5	1.5 (0.1)	1.4	3.5 (0.1)	0.8	2.64 (0.08)
CaO	10.7	9.6	9.6 (0.1)	7.7	8.5 (0.3)	9.5	6.79 (0.07)
Na_2O	3.7	3.2	3.5 (0.1)	3.5	3.0 (0.1)	0.3	3.27 (0.03)
K_2O	0.5	0.8	0.73 (0.02)	1.2	0.74 (0.04)	0.2	1.17 (0.02)
P_2O_5	0.1	0.2	0.21 (0.02)	0.3	0.16 (0.03)	1.0	0.22 (0.02)
Total[a]	93.9	96.6	96.7	98.0	94.5 (0.4)	94.8	94.7 (0.4)
TAS content	4.2	4.0	4.2	5.2	3.8	4.0	4.4
H_2O content[c]	3.5	3.0	2.9	1.8	4.5	3.9	3.5

Notes. [a]See Table 5. [b]Original total in wt. %. [c]H_2O calculated by mass balance and mixed H2O-CO2 solubility model of Shishkina et al. (2010) and Dixon et al. (2008). FeO = total Fe expressed as Fe^{2+}. Numbers in parentheses refer to 1s of the mean of multiple analyses. Where the 1s is less than the relative error, the relative error is reported instead. TAS = Total Alkali-Silica content.*

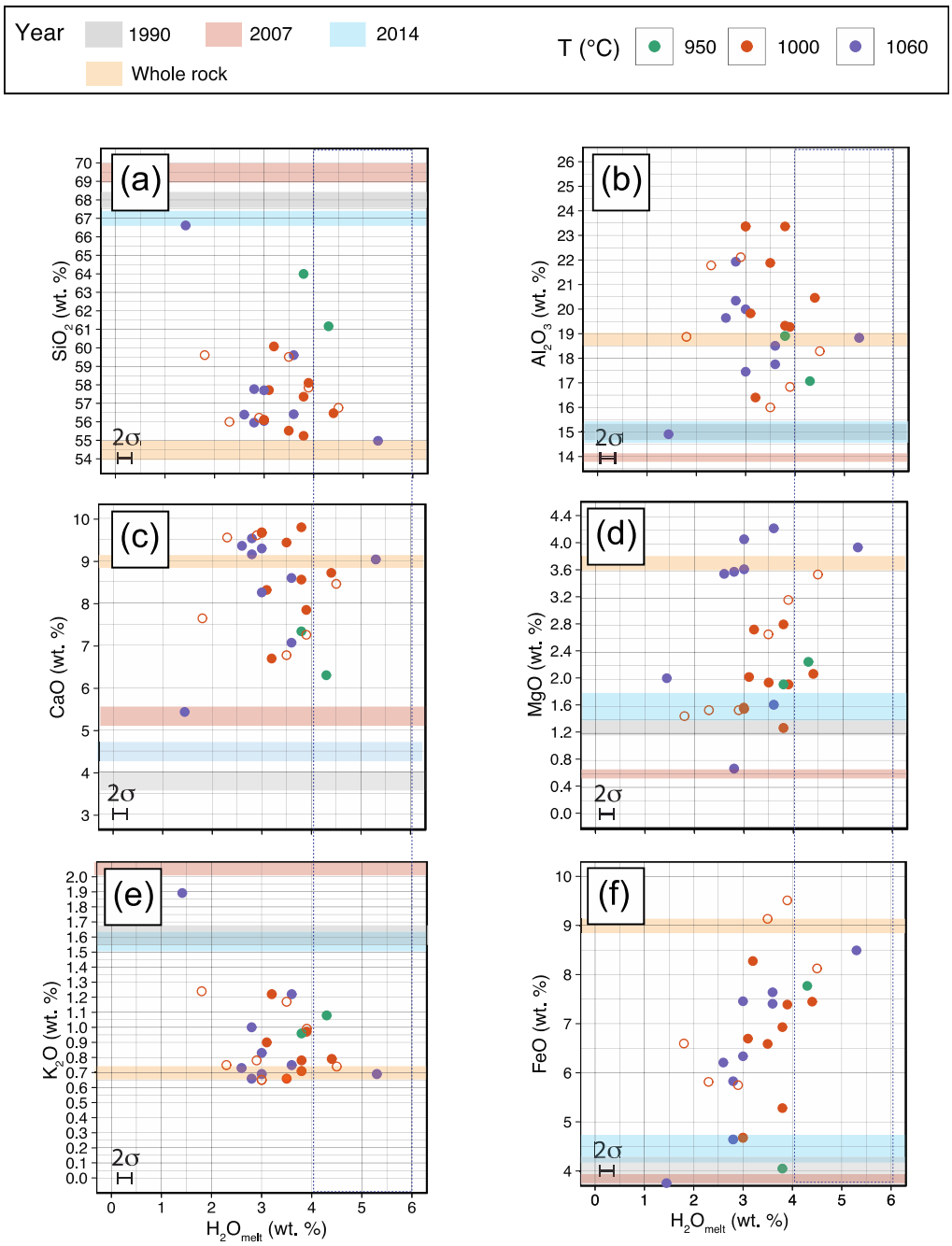

523

524 ***Figure 5*** *Major element oxide compositions of experimental glasses (in wt. %) vs. dissolved*
525 *water content in the melt for* ***a.*** *SiO_2,* ***b.*** *Al_2O_3,* ***c.*** *CaO,* ***d.*** *MgO,* ***e.*** *K_2O,* ***f.*** *FeO*. Solid coloured*
526 *boxes denote the range of whole rock and glass compositions reported in Utami et al. (in*
527 *revision) and this study for all three eruptions. The glass composition for the 2007 dome sample*
528 *was estimated by mass balance calculations (Albarede, 1995). The dashed blue square denotes*
529 *the pre-eruptive water content in the melt.*

530

531 4.4.2 Plagioclase

532 It was difficult to obtain "pure" analyses of experimental plagioclase due to its elongated
533 shape (e.g. very thin in one direction) and the presence of various mineral inclusions, so we
534 report the recalculated analyses after subtraction of the effect of mineral inclusions (see
535 methodology section). We first filtered the experimental Plag analyses for their FeO* and TiO_2
536 contents to remove Mag inclusions, but the MgO remained higher than expected for a
537 plagioclase (~1 wt. %). We thus suspect that there may be some analysis that are mixtures of
538 Plag and Opx, which we have not attempt to correct further. However, this should not affect the
539 relative Ca-Na-K concentrations and thus determination of the stoichiometric Plag end-members.
540 Experimental plagioclase ranges in composition from about An_{57} to An_{71} (Table 7; Fig 6a), and
541 varies according to the water content in the melt and to a lesser extent, by temperature. For the
542 same *T*, *P* and fO_2, we find that water content positively correlates with An content. We have not
543 been able to analyze experimental Plag for near liquidus charges, nor from those with very high
544 crystal content. Some of the experimental Plag compositions overlap with natural Plag microlites
545 and rims from the 1990, 2007, and 2014 eruptions as described in Utami et al. (in revision) and
546 in this study with An_{59-71} (Fig. 6a-c; Table S1). Specifically, microlites and phenocryst rims from
547 the 1990-2014 eruptions (An from 65 to 68) overlap with experimental Plag crystallized at 200
548 MPa, 1000°C and ΔNNO with ~4 wt. % water. No experimental Plag composition that we
549 analyzed have An content > 71. However, we find that Plag cores and some oscillatory growth
550 zones from all three eruptions with An content of > 71 in this study, Utami et al. (in revision),
551 and in Cassidy et al. (2016) (See Fig. 1 and Fig. S3 of Supplementary Data). Thermodynamic
552 modelling with rhyolite-MELTS at 975°C and 4 wt. % water shows that Plag with An content of
553 85-90 can be produced within the range of experimental temperatures (962-1062°C).
554

555 **Table 7:** *Experimental plagioclase chemistry*.
556

T (°C)	1000	1000	1000	950	950	1060	1060	1000	1000	1000	1000	950	950	950	950
Charge	SUPL1-11N	SUPL1-12N	SUPL1-13N	SUPL1-28N	SUPL1-30	SUPL1-44N	SUPL1-45N	SUPL1-58N	SUPL1-59N	SUPL1-60N	SUPL1-61N	SUPL1-63	SUPL1-64	SUPL1-65N	SUPL1-66
n	2	1	2	1	3	1	1	1	2	3	2	3	3	2	1
wt. %															
SiO_2	57.9	59.0	57.5	59.9	54.8 (0.1)	59.2	58.7	58.4	59.9	57.9	62.0	58 (1)	53 (1)	58.6	55.7
TiO_2					0.2 (0.1)	0.2					0.01	0.2 (0.1)	0.06 (0.02)		0.1
Al_2O_3	25.6	24.1	26.3	23.1	26.4 (0.6)	23.5	25.6	24.6	23.0	25.9	22.4	26 (1)	29.7 (0.6)	24.3	27.3
FeO*	0.2	0.6	0.1	1.1	1.9 (1)	1.1	0.2	0.8	1.1	0.03	0.6	1.4 (0.5)	1.1 (0.1)	1.2	1.1
MnO	0.1	0.2	0.0	0.2	0.05 (0.01)	0.1	0.1	0.1	0.1	0.05	0.1	0.03 (0.02)	0.02 (0.01)	0.1	0.02
MgO	1.4	1.4	0.9	3.3	0.6 (0.2)	1.1	0.5	1.6	1.6	0.8	1.2	0.3 (0.1)	0.14 (0.3)	1.4	0.2
CaO	11.1	10.5	11.4	9.5	10.7 (0.4)	10.5	11.0	11.0	10.2	11.4	8.7	10 (1)	13.2 (0.7)	10.3	11.1
Na_2O	3.3	3.6	3.7	3.6	3.6 (0.1)	3.5	3.9	3.5	3.8	3.9	3.8	3.5 (0.3)	3.09 (0.03)	3.6	3.5
K_2O	0.5	0.7	0.5	0.4	0.3 (0.1)	0.9	0.7	0.7	0.8	0.6	1.2	0.5 (0.2)	0.14 (0.04)	0.5	0.4
Total[a]	97.5 (0.5)	97.9	98.4 (0.1)	98.3	98.4 (0.5)	97.1	98.0	98.7	98 (1)	98.2 (0.5)	98.4 (0.6)	99.9 (1)	100.5 (0.4)	99.2 (0.6)	99.4
Plag end-member															
An	63.9 (0.5)	58.8	61 (2)	58	61 (2)	60.4	58.5	61.0	57 (1)	59.3 (0.4)	53 (5)	59 (2)	70 (1)	59 (2)	62.0
Ab	32.6 (0.4)	36.6	36 (1)	39	37 (1)	34.2	36.8	34.9	37.8 (0.5)	37 (1)	39 (3)	38 (1)	30 (1)	37.0 (0.8)	35.4
Or	3.5 (0.1)	4.5	4 (1)	3	2 (0.4)	5.4	4.7	4.1	5.3 (0.1)	4 (1)	8 (2)	3 (1)	0.8 (0.3)	3.6 (0.9)	2.6

557

558 *Notes. FeO* = total Fe expressed as Fe^{2+}. Numbers in parentheses refer to 1s of the mean of multiple analyses. n = calculated and*
559 *normalized plagioclase composition after subtraction of Fe-Ti oxide composition. [a]Original total oxide in wt. %. See Table 3 for end-*
560 *member abbreviations and calculations.*
561
562

563

564 4.4.3 Orthopyroxene

565 Experimental Opx composition mainly varies with temperature and water content in the
566 melt (Mg # 57-77; Fig 6b, Table 8). The Wo component of some of the experimental Opx is high
567 (Wo_{6-11}), and is classified as pigeonite according to Deer et al. (1992). For the same *P* and fO_2, a
568 temperature increase from 950°C to 1000°C results in an increase in the Mg # of about 58 to 70;
569 a decrease in water content in the melt also results in an increase in Mg #. A strong influence of
570 water content in the Opx-melt Mg # partitioning was reported in previous experimental studies
571 (Waters & Lange, 2017). The 1990, 2007, and 2014 Opx cores and glomerocrysts range from
572 Mg # 66 to 76 (average of 66), with a bimodal distribution. This Mg # range overlaps with
573 experimental orthopyroxene compositions at 1000°C, 200 MPa and at NNO for all eruptions,
574 although we have not identified pigeonite in the natural samples.
575

576 4.4.4 Clinopyroxene

577 Experimental Cpx is ubiquitous in most charges (Mg # 61-76, $Wo_{33-40}En_{39-46}Fs_{15-25}$) (Fig
578 6c, Table 8). The Mg # of experimental Cpx increases from 61 to 76 with increasing
579 temperature. There appears to be some effect of water content on composition: at 950°C, the
580 experimental Cpx at 200 MPa have higher Mg # (68-69) than at 400 MPa (61-63). As we could
581 not obtain good quantitative analysis of Cpx for all charges, we have no clear indication of the
582 effect of fO_2 on clinopyroxene composition. The 1990, 2007, and 2014 clinopyroxene cores and
583 glomerocrysts composition Mg # (70-76, average ~ 74) overlap with experimental clinopyroxene
584 at 1000°C, 200 MPa, and NNO + 2 at 4 wt. % water.
585
586

587 **Table 8.** *Experimental pyroxene chemistry*
588

Mineral	Pgt	Opx	Opx	Pgt	Opx	Pgt	Opx	Pgt	Pgt	Opx	Opx	Opx
T (°C)	1000	1000	1000	1000	1000	1000	1000	1000	1000	1000	1000	950
Charge	SUPL 1-02	SUPL 1-11	SUPL 1-12	SUPL 1-12	SUPL1 -13	SUPL 1-13	SUPL1 -16	SUPL 1-16	SUPL 1-17	SUPL 1-18	SUPL 1-19	SUPL 1-31
n:	3	6	14	1	4	1	5	1	1	1	3	3
wt. %												
SiO_2	52.0 (1.1)	52.6 (0.8)	52.5 (0.5)	52.1	54.0 (1.0)	52.7	51.0 (0.8)	49.8	51.5	50.1	51.1 (0.6)	51.0 (0.3)
TiO_2	0.29 (0.02)	0.24 (0.04)	0.27 (0.04)	0.3	0.16 (0.03)	0.2	0.31 (0.07)	0.3	0.2	0.3	0.30 (0.07)	0.34 (0.01)
Al_2O_3	1.6 (0.5)	2.3 (0.9)	2.0 (0.3)	2.6	2.7 (0.6)	0.7	4 (1)	6.0	1.2	2.6	2.1 (0.8)	2.6 (0.2)
Cr_2O_3	0.05 (0.02)	0.03 (0.02)	0.51 (0.05)	0.1	0.5 (0.1)	0.03	0.10 (0.03)	0.1	0.05	b.d.	0.10 (0.04)	0.14 (0.03)
FeO*	20.9 (0.4)	18.9 (0.7)	20.0 (0.6)	18.2	14.1 (0.1)	22.3	20.9 (0.6)	20.2	22.0	24.8	22.2 (0.3)	24.6 (0.2)
MnO	0.7 (0.1)	0.58 (0.03)	0.63 (0.01)	0.6	0.47 (0.02)	0.7	0.58 (0.03)	0.6	0.7	0.6	0.64 (0.04)	0.65 (0.03)
MgO	18.6 (0.5)	22.7 (0.7)	21.9 (0.3)	21.0	25.7 (0.6)	19.4	19.4 (0.6)	18.7	18.4	19.5	19.1 (0.6)	18.1 (0.4)
CaO	5.4 (0.2)	2.2 (0.3)	2.0 (0.2)	3.9	2.3 (0.2)	3.8	2.6 (0.5)	3.1	4.4	2.2	3 (1)	1.8 (0.1)
Na_2O	0.2(0.2)	b.d.	b.d.	0.1	0.04 (0.03)	0.05	0.2 (0.1)	0.4	0.1	b.d.	0.05 (0.02)	0.03 (0.01)
K_2O	0.05 (0.06)	0.02 (0.02)	b.d.	b.d.	b.d.	0.01	0.01 (0.01)	0.0	0.01	b.d.	b.d.	b.d.
Total	99.7 (1.4)	99.6 (1.2)	99.5 (0.5)	98.8	100.0 (0.6)	100.0	99.1 (0.6)	99.1	98.4	100.1	98.5 (0.3)	99.1 (0.6)
Mg #[a]	61.4 (1.1)	68 (2)	66.2 (0.9)	67.2	76.5 (0.5)	60.8	62.3 (0.7)	62.3	59.9	58.3	60.5 (0.5)	56.7 (0.7)
End-member[a]												
Wo	11.4 (0.3)	5 (1)	4.2 (0.4)	8.3	4.7 (0.5)	7.9	6 (1)	7.0	9.3	4.4	6 (3)	3.8 (0.2)
En	54.4 (0.8)	65 (2)	63.4 (0.9)	61.6	72.9 (0.8)	56.0	58.7 (0.9)	58.0	54.3	55.7	57 (2)	54.5 (0.8)
Fs	34.2 (1.1)	30 (1)	32.4 (0.9)	30.1	22.4 (0.4)	36.1	35.5 (0.8)	35.0	36.4	39.8	37.0 (0.6)	41.6 (0.6)

Mineral	Opx	Opx	Opx	Pgt	Pgt	Opx	Opx	Opx	Opx	Opx	Opx	Opx
T (°C)	950	950	950	1060	1060	1060	1060	1060	1060	1000	1000	1000
Charge	SUPL 1-32	SUPL 1-33	SUPL 1-34	SUPL 1-44	SUPL1 -45	SUPL 1-46	SUPL1 -46	SUPL 1-49	SUPL 1-50	SUPL 1-51	SUPL 1-57	SUPL 1-59
n:	10	6	7	1	1	1	1	9	1	26	1	3
wt. %												
SiO_2	51.3 (0.6)	51.5 (0.4)	51.8 (0.2)	52.9	53.7	53.7	53.9	52.7 (1.0)	53.1	53.0 (0.9)	52.0	53.1 (0.9)
TiO_2	0.36 (0.05)	0.37 (0.03)	0.38 (0.04)	0.3	0.1	0.1	0.2	0.20 (0.02)	0.3	0.23 (0.04)	0.3	0.23 (0.05)
Al_2O_3	2.4 (0.5)	2.3 (0.4)	2.5 (0.5)	2.4	1.1	1.1	1.8	3.6 (0.7)	2.6	2.1 (0.7)	2.4	3 (1)
Cr_2O_3	0.11 (0.04)	0.13 (0.01)	0.10 (0.03)	0.0	0.2	0.2	0.2	0.4 (0.4)	0.5	0.04 (0.03)	0.2	0.29 (0.07)
FeO*	23.8 (0.2)	24.0 (0.2)	23.4 (0.3)	22.0	18.9	18.9	19.1	14.7 (0.8)	17.9	17.3 (0.5)	19.5	17.3 (0.2)
MnO	0.65 (0.02)	0.66 (0.02)	0.67 (0.03)	0.7	0.6	0.6	0.7	0.46 (0.03)	0.6	0.58 (0.03)	0.6	0.55 (0.05)
MgO	18.6 (0.2)	18.5 (0.2)	18.9 (0.4)	19.9	22.9	22.9	20.6	25.6 (0.4)	21.9	24.2 (0.9)	22.1	23.5 (0.5)
CaO	1.9 (0.2)	2.1 (0.1)	2.0 (0.2)	2.9	3.3	3.3	4.6	2.2 (0.3)	3.3	2.1 (0.4)	2.1	2.1 (0.9)

Na_2O	0.03 (0.01)	0.06 (0.04)	0.06 (0.05)	0.3	0.1	0.1	0.2	b.d.	0.05	b.d.	0.01	0.04 (0.02)
K_2O	b.d.	0.01 (0.01)	0.01 (0.01)	0.03	0.01	0.01	0.01	b.d.	0.01	b.d.	0.03	0.01 (0.01)
Total	99.1 (0.3)	99.5 (0.5)	99.8 (0.4)	101.5	101.0	101.0	101.3	100.2 (0.6)	100.1	100 (1)	99.4	99.9 (0.3)
Mg #[a]	58.2 (0.3)	57.8 (0.2)	59.0 (0.3)	61.7	68.4	68.4	65.8	75.6 (1.0)	68.6	71.4 (0.9)	66.9	70.8 (0.3)
End-member[a]												
Wo	4.0 (0.5)	4.5 (0.3)	4.3 (0.5)	6.1	6.5	6.5	9.5	4.5 (0.6)	6.9	4.3 (0.8)	4.4	4 (2)
En	55.8 (0.4)	55.2 (0.2)	56.5 (0.6)	57.9	63.9	63.9	59.5	72.1 (0.9)	63.9	68 (1)	64.0	68 (1)
Fs	40.1 (0.2)	40.3 (0.2)	39.2 (0.2)	36.0	29.6	29.6	31.0	23.3 (1.0)	29.3	27.4 (0.8)	31.6	28.0 (0.4)

Mineral	Opx	Opx	Pgt	Cpx	Cpx	Cpx	Cpx	Cpx	Cpx	Cpx	Opx	Opx
T (°C)	1000	950	950	1000	950	950	950	1000	1000	950	1060	1000
Charge	SUPL 1-61	SUPL 1-64	SUPL 1-29	SUPL 1-18	SUPL1 -28	SUPL 1-31	SUPL1 -34	SUPL 1-58	SUPL 1-59	SUPL 1-64	SUPL 1-50	SUPL 1-51
n:	1	7	1	3	4	1	5	3	3	1	1	26
wt. %												
SiO_2	52.2	53.6 (0.7)	52.6	48.9 (0.6)	52.6 (0.9)	50.1	50.7 (0.6)	52 (1)	51.7 (0.6)	53.3	53.1	53.0 (0.9)
TiO_2	0.3	0.24 (0.05)	0.3	0.62 (0.09)	3.1 (0.6)	0.7	0.72 (0.06)	0.4 (0.1)	0.5 (0.1)	0.4	0.3	0.23 (0.04)
Al_2O_3	2.6	2.2 (0.5)	2.4	5.0 (0.3)	19 (2)	3.2	3.3 (0.2)	3.0 (0.9)	3.1 (0.3)	4.4	2.6	2.1 (0.7)
Cr_2O_3	0.3	0.02 (0.01)	0.01	0.10 (0.06)	b.d.	0.3	0.22 (0.01)	0.4 (0.1)	0.5 (0.1)	0.02	0.5	0.04 (0.03)
FeO*	19.4	18.1 (0.2)	17.7	10.1 (0.3)	14 (1)	14.3	13.1 (0.9)	9.2 (0.1)	10 (2)	10.8	17.9	17.3 (0.5)
MnO	0.6	0.70 (0.05)	0.7	0.40 (0.05)	0.25 (0.01)	0.5	0.4 (0.1)	0.4 (0.1)	0.4 (0.1)	0.5	0.6	0.58 (0.03)
MgO	21.3	22.0 (0.4)	21.5	14.4 (0.5)	0.4 (0.1)	12.7	12.8 (0.1)	15.9 (0.8)	15 (2)	13.2	21.9	24.2 (0.9)
CaO	2.7	3.1 (0.3)	5.0	18.3 (0.8)	19 (2)	16.5	18 (1)	18.4 (0.5)	18 (3)	17.6	3.3	2.1 (0.4)
Na_2O	0.1	0.06 (0.01)	0.1	0.28 (0.02)	0.255 (0.01)	0.2	0.24 (0.03)	0.19 (0.02)	0.20 (0.04)	0.3	0.05	b.d.
K_2O	0.02	0.02 (0.01)	0.01	0.03 (0.02)	0.5 (0.1)	0.01	0.04 (0.02)	0.03 (0.01)	b.d.	0.1	0.01	b.d.
Total	99.5	100.1 (0.5)	100.3	98.1 (0.2)	101.3 (0.3)	98.4	99.3 (0.8)	100.0 (0.6)	99.7 (0.5)	100.7	100.1	100 (1)
Mg #[a]	66.3	68.4 (0.4)	68.4	71.9 (0.9)	69 (1)	61.3	63.4 (0.7)	76 (1)	73 (1)	68.6	68.6	71.4 (0.9)
End-member[a]												
Wo	5.8	6.5 (0.6)	10.3	40 (1)	39 (3)	36	39 (3)	39 (1)	38 (7)	39.6	6.9	4.3 (0.8)
En	62.4	64.0 (0.7)	61.4	43 (1)	42 (3)	39	39 (1)	46 (2)	45 (4)	41.5	63.9	68 (1)
Fs	31.8	29.5 (0.4)	28.3	17 (1)	19 (1)	25	22 (1)	15.0 (0.3)	17 (3)	19.0	29.3	27.4 (0.8)

Mineral[1]	Opx	Pgt	Opx	Opx	Opx	Cpx	Cpx	Cpx	Cpx	Cpx	Cpx	Cpx
T (°C)	1000	1000	1000	1000	950	1000	950	950	950	1000	1000	950
Charge	SUPL 1-57	SUPL 1-57	SUPL 1-59	SUPL 1-61	SUPL1 -64	SUPL 1-18	SUPL1 -28	SUPL 1-31	SUPL 1-34	SUPL 1-58	SUPL 1-59	SUPL 1-64

n:	1	1	3	1	7	3	4	1	5	3	3	1
wt. %												
SiO_2	52.0	52.6	53.1 (0.9)	52.2	53.6 (0.7)	48.9 (0.6)	52.6 (0.9)	50.1	50.7 (0.6)	52 (1)	51.7 (0.6)	53.3
TiO_2	0.3	0.3	0.23 (0.05)	0.3	0.24 (0.05)	0.62 (0.09)	3.1 (0.6)	0.7	0.72 (0.06)	0.4 (0.1)	0.5 (0.1)	0.4
Al_2O_3	2.4	1.5	3 (1)	2.6	2.2 (0.5)	5.0 (0.3)	19 (2)	3.2	3.3 (0.2)	3.0 (0.9)	3.1 (0.3)	4.4
Cr_2O_3	0.2	0.2	0.29 (0.07)	0.3	0.02 (0.01)	0.10 (0.06)	b.d.	0.3	0.22 (0.01)	0.4 (0.1)	0.5 (0.1)	0.02
FeO*	19.5	18.7	17.3 (0.2)	19.4	18.1 (0.2)	10.1 (0.3)	14 (1)	14.3	13.1 (0.9)	9.2 (0.1)	10 (2)	10.8
MnO	0.6	0.7	0.55 (0.05)	0.6	0.70 (0.05)	0.40 (0.05)	0.25 (0.01)	0.5	0.4 (0.1)	0.4 (0.1)	0.4 (0.1)	0.5
MgO	22.1	20.3	23.5 (0.5)	21.3	22.0 (0.4)	14.4 (0.5)	0.4 (0.1)	12.7	12.8 (0.1)	15.9 (0.8)	15 (2)	13.2
CaO	2.1	5.0	2.1 (0.9)	2.7	3.1 (0.3)	18.3 (0.8)	19 (2)	16.5	18 (1)	18.4 (0.5)	18 (3)	17.6
Na_2O	0.01	0.06	0.04 (0.02)	0.1	0.06 (0.01)	0.28 (0.02)	0.255 (0.01)	0.2	0.24 (0.03)	0.19 (0.02)	0.20 (0.04)	0.3
K_2O	0.03	0.01	0.01 (0.01)	0.02	0.02 (0.01)	0.03 (0.02)	0.5 (0.1)	0.01	0.04 (0.02)	0.03 (0.01)	b.d.	0.1
Total	99.4	99.2	99.9 (0.3)	99.5	100.1 (0.5)	98.1 (0.2)	101.3 (0.3)	98.4	99.3 (0.8)	100.0 (0.6)	99.7 (0.5)	100.7
Mg #[a]	66.9	65.9	70.8 (0.3)	66.3	68.4 (0.4)	71.9 (0.9)	69 (1)	61.3	63.4 (0.7)	76 (1)	73 (1)	68.6
End-member[a]												
Wo	4.4	10.5	4 (2)	5.8	6.5 (0.6)	40 (1)	39 (3)	36	39 (3)	39 (1)	38 (7)	39.6
En	64.0	59.0	68 (1)	62.4	64.0 (0.7)	43 (1)	42 (3)	39	39 (1)	46 (2)	45 (4)	41.5
Fs	31.6	30.5	28.0 (0.4)	31.8	29.5 (0.4)	17 (1)	19 (1)	25	22 (1)	15.0 (0.3)	17 (3)	19.0

Notes. [a]Pyroxene end-members and Mg # calculations are as in Table 3. FeO = total Fe expressed as Fe^{2+}. Pgt: pigeonite. b.d. = below detection level. Numbers in parentheses refer to 1s of the mean of multiple analyses. Where the 1s is less than the relative error, the relative error is reported instead.*

596

597 4.4.5 Olivine

598 Experimental Ol (100-500 μm) is present in charges at 950-1000°C, P = 100-150 MPa at NNO,
599 and 1000°C, 200 MPa, at NNO + 2 (Fig. 6d, Table 9). Its Fo content ranges from 59 to 76, and
600 increases with temperature for a water content of 3-5 wt. %. There is no systematic change in Fo
601 with increasing fO_2 from NNO to NNO + 2. We can only compare the experimental Ol
602 compositions to Ol from the 2014 eruption, because the Ol from the 1990 and 2007 eruptions
603 have completely reacted to symplectites. There are two compositional groups of Ol from the
604 2014 eruption, with one at Fo = 72-75 and another at Fo = 67-69. The high-Fo group of Ol
605 overlaps with experimental Ol from 100 MPa, 1060°C and NNO and ~3 wt. % water, and the
606 low-Fo group overlap with experimental Ol from 60°C lower.
607

608 4.4.6 Amphibole

609 It was particularly difficult to identify Amph in the experimental charges, and we were
610 able to obtain good quantitative analysis of one experimental Amph (magnesio-hornblende; Mg
611 # = 69; Table 9) in the charge at 950°C, 400 MPa, and 6 wt. % dissolved water in the melt (Fig.
612 2g-h). We also identified additional Amph crystals in other charges using principal component
613 analyses of mineral compositions obtained with the electron microprobe analysis (Fig. S2). The
614 geothermobarometry results from the natural Amph of the 1990 and 2014 eruptions agree with
615 the experimental Amph stability field we have found (Fig. 4). We reconstructed the composition
616 melt from natural Amph from 1990 and 2014 according to the methodology of Li et al. (2021) to
617 compare the equilibrium SiO_2 content of the parental melt of Amph with that of our glasses. We
618 find that the Al/Si ratio of Amph from 1990 correspond to 53-60 wt. %, which is close to the
619 SiO_2 content of the starting material glass. The equilibrium melt of Amph from 2014 is more
620 silica-rich, with 68-70 wt. % SiO_2, which overlaps with the interstitial glasses. This suggests that
621 the Amph from 1990 and 2014 came from different melts, where the 1990 Amph was sampled
622 from a less differentiated melt than the 2014 Amph.
623
624

4.4.7 Fe-Ti oxides

Magnetite and ilmenite crystallized in experimental charges depending on the water content in the melt, and magnetite is more common (Table 10). Experimental magnetite (X_{usp} = 0.24-0.60) is present in almost all water-saturated charges. Ilmenite occurs in water poor charges. Although we have identified ilmenite in charges through its EDS spectrum, we were not able to quantitatively determine their compositions.

Table 9. *Experimental amphibole and olivine compositions*

Mineral[a]	Amph	Amph	Amph	Amph	Ol	Ol	Ol	Ol	Ol	Ol	Ol
T (°C)	1000	1000	950	950	1000	1000	950	1060	1060	1000	1000
Charge	SUPL1-16	SUPL1-17	SUPL1-32	SUPL1-28	SUPL1-1	SUPL1-6	SUPL1-21	SUPL1-38	SUPL1-39	SUPL1-58	SUPL1-59
n:	1	1	1	1	7	1	1	1	2	3	3
wt. %											
SiO_2	48.5	48.9	48.6	52.2	37.2 (0.4)	36.3	36.2	37.5	37.9 (0.5)	38.0 (0.4)	37.5 (0.4)
TiO_2	0.6	0.9	0.5	0.5	0.02 (0.01)	0.02	0.02	0.05	0.02 (0.01)	0.02 (0.01)	0.02 (0.01)
Al_2O_3	4.5	10.1	5.3	4.0	0.2 (0.2)	0.02	0.02	0.03	0.04 (0.01)	0.03 (0.01)	b.d.
Cr_2O_3	0.1			0.1	b.d.	0.01	b.d.	0.02	0.04 (0.02)	b.d.	b.d.
FeO*	14.6	11.9	15.3	18.4	27.8 (0.2)	27.7	34.1	21.8	21.6 (0.2)	25.1 (0.2)	28.5 (0.3)
MnO	0.4	0.4	0.5	0.6	0.65 (0.02)	0.6	0.8	0.5	0.51 (0.01)	0.53 (0.02)	0.58 (0.01)
MgO	13.1	11.0	15.9	11.9	33.6 (0.2)	32.7	28.1	38.1	38.4 (0.4)	35.7 (0.1)	32.7 (0.3)
CaO	15.7	16.4	12.1	12.7	0.3 (0.1)	0.2	0.2	0.3	0.28 (0.03)	0.23 (0.01)	0.27 (0.4)
Na_2O	0.7	1.2	0.3	0.3	b.d.	0.001	0.01	0.01	0.01 (0.01)	b.d.	b.d.
K_2O	0.2	0.1	0.0	0.1	b.d.	0.03	0.01	0.01	0.01 (0.01)	b.d.	b.d.
Total	98.5	100.7	98.5	100.8	99.4 (0.5)	97.4	99.2	98.1	98.6 (0.7)	99.4 (0.04)	99.4 (0.1)
End-member[a]	Mg-hbl	und.	Mg-hbl	Mg-hbl							
Mg #[a]	61.5	62.2	68.7	53.6							
Fo content[a]					68.3 (0.2)	67.8	59.5	75.7	76 (1)	71.7 (0.2)	66.9 (0.3)

Notes. See Table 2 for meaning of abbreviations. Mg-hbl = Magnesio-hornblende. FeO = total Fe expressed as Fe^{2+}. Mg # = 100 x Mg / (Mg + Fe*). b.d. = composition below detection level.*

und. = undetermined. Numbers in parentheses refer to 1s of the mean of multiple analyses. Where the 1s is less than the % error, the % error is reported instead.

Table 10: *Experimental Fe-Ti oxides chemistry.*

T (°C)	1000	1000	1000	1000	1000	1000	1000
Charge	SUPL1-1	SUPL1-2	SUPL1-3	SUPL1-12	SUPL1-13	SUPL1-14	SUPL1-15
n:	1	1	3	3	7	8	3
wt .%							
SiO_2	0.5	0.3	0.30 (0.07)	0.30 (0.08)	0.21 (0.03)	0.3 (0.1)	0.3 (0.1)
TiO_2	5.2	11.5	10.9 (0.5)	8.1 (0.1)	9.0 (0.3)	13.2 (0.1)	16.9 (0.1)
Al_2O_3	5.7	3.3	3.5 (0.1)	5.3 (0.1)	4.8 (0.1)	3.8 (0.1)	3.1 (0.1)
FeO*	67.0	71.8	70.8 (0.7)	71.4 (0.2)	70.5 (0.7)	70.0 (0.2)	63.8 (0.2)
MnO	0.5	0.4	0.47 (0.02)	0.42 (0.01)	0.46 (0.01)	0.46 (0.01)	0.51 (0.01)
MgO	3.7	2.4	2.37 (0.04)	3.05 (0.02)	2.8 (0.1)	2.43 (0.03)	2.1 (0.1)
CaO	0.2	0.3	0.24 (0.03)	0.2 (0.1)	0.15 (0.01)	0.20 (0.04)	0.25 (0.02)
Total	82.8	90.0	88.6 (0.8)	88.8 (0.3)	88.0 (0.8)	90.4 (0.2)	86.93 (0.02)
FeO^c	54.0	59.2	58.4 (0.5)	57.7 (0.1)	57.5 (0.5)	58.3 (0.1)	55.3 (0.1)
Fe_2O_3	14.5	14.1	13.8 (0.2)	15.2 (0.1)	14.5 (0.2)	13.0 (0.1)	9.5 (0.1)
X_{usp}	0.24	0.38	0.37(0.01)	0.28 (0.01)	0.31 (0.01)	0.44 (0.01)	0.58 (0.01)

T (°C)	950	950	950	950	950	950	950	950
Charge	SUPL1-28	SUPL1-29	SUPL1-30	SUPL1-31	SUPL1-32	SUPL1-64	SUPL1-65	SUPL1-67
n:	1	1	1	1	1	1	1	2
wt .%								
SiO_2	0.3	0.4	0.6	0.4	0.3	0.3	0.3	0.2 (0.1)
TiO_2	15.8	16.2	16.7	15.1	16.0	16.3	7.5	12.0 (0.7)
Al_2O_3	2.9	2.6	2.7	2.7	4.5	2.6	3.8	3.00 (0.05)
FeO*	70.9	68.6	64.8	69.9	63.9	67.0	75.9	72.4 (0.9)
MnO	0.3	0.4	0.4	0.5	0.5	0.4	0.5	0.41 (0.02)
MgO	0.7	1.4	1.4	1.7	2.2	1.4	1.8	1.52 (0.01)
CaO	0.3	0.2	0.3	0.4	0.3	0.3	0.3	0.30 (0.03)
Total	91.2	89.9	87.0	90.7	87.8	88.4	90.3	90 (1)
FeO^c	57.7	58.8	56.4	59.1	55.0	60.5	61.4	60.2 (0.6)
Fe_2O_3	10.4	10.9	9.3	12.1	9.9	11.5	16.2	13.7 (0.3)
X_{usp}	0.50	0.53	0.57	0.49	0.55	0.54	0.25	0.39 (0.01)

Notes. Fe_2O_3 calculated using the approach by Droop (1987), where $Fe_2O_3 = FeO^* \times (Fe^{3+} / Fe^{2+} + Fe^{3+}) \times 1.1113$. $FeO^c = FeO$ calculated using the approach by Droop (1987) ,where $FeO^c = FeO^* \times (Fe^{2+} / Fe^{2+} + Fe^{3+})$. Numbers in parentheses refer to 1s of the mean of multiple

analyses. Where the 1s is less than the relative error, the relative error is reported instead. b.d. = below detection level.

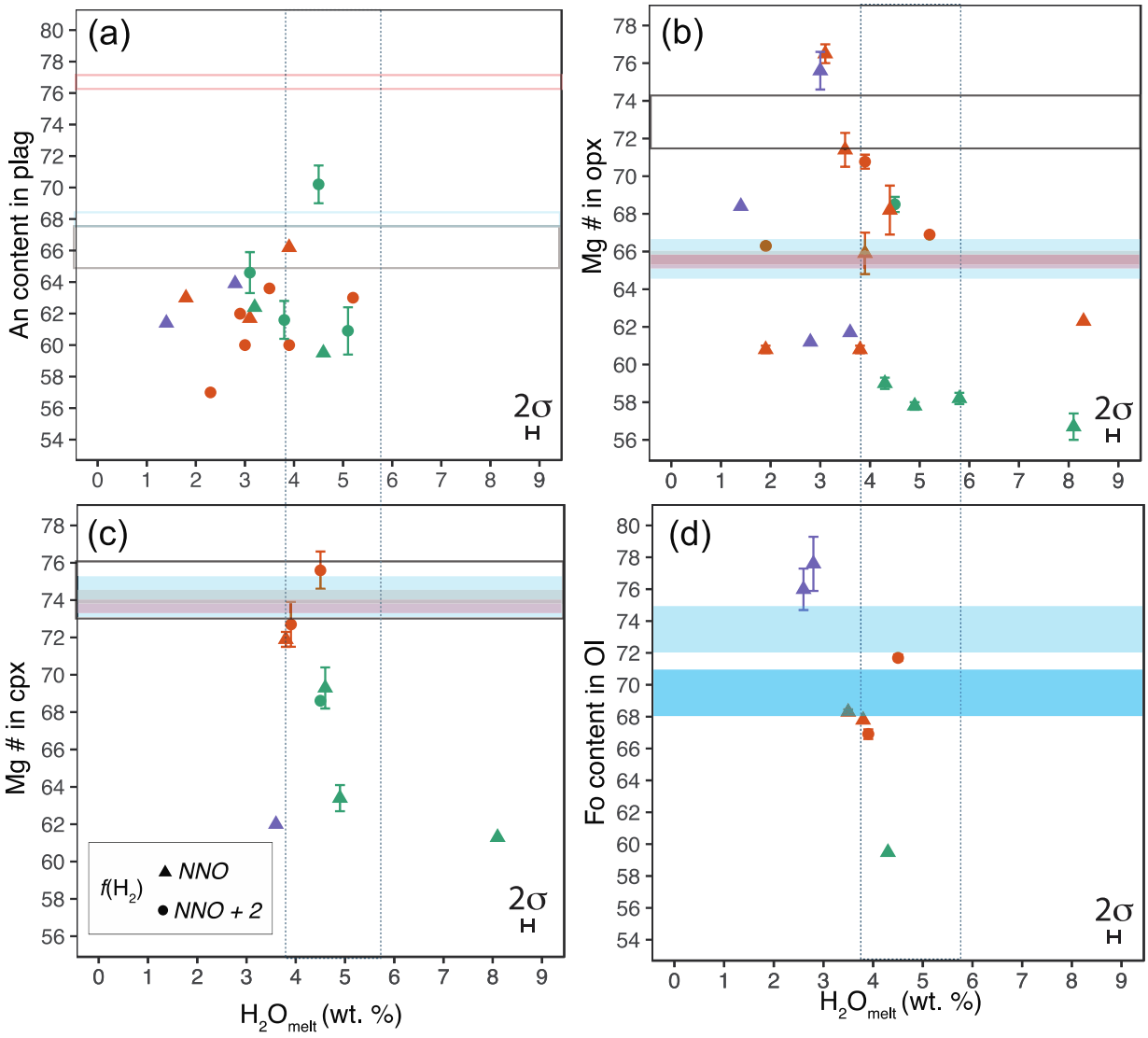

Figure 6. *Variations in experimental mineral compositions of experimental charges compared to natural ones (Plag, Cpx, Opx, and Ol) of the crystal cargo of 1990, 2007, and 2014 eruptions:* ***a.*** *An in Plag,* ***b.*** *Mg # in Opx,* ***c.*** *Mg # in Cpx, and* ***d.*** *Fo content in Ol. Coloured solid boxes denote the observed ranges of mineral compositions from the three eruptions, with the same colours as outlined in Fig. 5. Open boxes represent rim compositions of the minerals (Utami et al. (in revision) and Table 2 of this study).*

655 **5 Discussion**

656 5.1 Geothermobarometry and experimental constraints on magma storage conditions of sub-
657 Plinian eruptions and dome extrusions

658 Combining the geothermobarometric and experimental results, we find that the pre-
659 eruptive magma storage conditions that match the phenocryst content, natural phase assemblage,
660 and some of the mineral compositions for the three eruptions are at 975 ± 39°C, 175 ± 25 MPa,
661 with 4-6 wt. % water in the melt and a fO_2 of NNO. These conditions correspond to about 7 km
662 of storage below the crater if we use a crustal density of 2640 kg m^{-3}. However, this does not
663 mean that all of the crystal cargo grew at this depth, as amphibole geobarometry indicates
664 pressures of up to 400 MPa (up to ~15 km), and hence some these crystals were probably
665 entrained from deeper parts of the magmatic system (Fig. 4a; Utami et al., in revision). A key
666 difference between the 1990 and 2014 eruptions and those of the 2007 dome is the much hugher
667 phenocryst content of the latter (Table 2). This could be due to crystal accumulation in the dome,
668 but the major and trace element compositions of the three eruptions are similar, including
669 incompatible trace elements such as Zr (this study; Jeffery et al., 2013), meaning that the
670 observed difference in crystal content is due to in situ crystallization. According to experimental
671 results, the lava dome's higher phenocryst content (Fig 3) can be reproduced with ~1 wt. %
672 water in the melt for a temperature of about 975°C. Thus we propose that the low apparent water
673 content is likely the result of additional storage at shallower pressures and/or transport towards
674 the surface that led to water loss and cooling, rather than a difference in the initial pre-eruptive
675 conditions. The presence of the pseudomorphs and symplectites that used to be Amph and Ol in
676 the 2007 rocks also indicate that the magma was originally stored at similar conditions to the
677 1990 and 2014 eruptions, although its slower ascent resulted in phenocryst proportions and
678 compositions to re-equilibrate to shallower depths.
679

680 5.2 The importance of excess volatiles in determining eruption style

681 The explosive → effusive → explosive eruption style transition shown by the 1990-2007-
682 2014 events remains some of the most intriguing aspects of Kelud volcano. Given that the pre-
683 eruptive or "initial" (e.g. before ascent) conditions of temperature, pressure, and water content in

684 the melt are broadly the same for the three events, other variables have played a role in
685 producing the different eruption styles. In Utami et al. (in revision), we proposed that the
686 explosive eruptions of the 1990 magma was likely due to excess fluid accumulation, and we
687 calculated that up to 0.12 Mt SO_2 could have resided as a separate fluid phase. Our mass balance
688 calculations for the SO_2 budget of the 2014 eruption also indicate the presence of an exsolved
689 volatile phase at pre-eruptive conditions, with up to 0.1 Mt SO_2 (Table 11). Such excess fluid can
690 be developed via progressive magma crystallization and volatile buildup to supersaturation (e.g.
691 Arzilli et al., 2019; Cassidy et al., 2019; Tramontano et al., 2017), with additional fluids can also
692 be due to fluid fluxing and degassing from a deep-seated basaltic magma reservoir and/or
693 limestone in the case of Kelud (e.g. Caricchi et al., 2018; Giuffrida et al., 2017; Utami et al., in
694 revision). Although we can only calculate the amount of SO_2, the fluid phase would have
695 certainly included water and CO_2. The presence of an exsolved fluid phase at pre-eruptive
696 conditions means that the magma buoyancy is greatly increased, as fluids can expand from the
697 moment the magma starts its ascent and lithospheric pressure decreases (Gonnermann & Manga,
698 2013). The additional buoyancy could lead to significantly faster magma ascent, depending on
699 the distribution of the fluid in the magma and whether there is a one- or two-phase flow, and also
700 lead to much higher explosivity.
701
702 Our hypothesis differs from that of Cassidy et al. (2019), who proposed that the
703 difference in eruption style is dependent on the degree of water saturation in the magma. They
704 further proposed that the 2007-2008 dome extrusion was triggered by an injection of hot, CO_2-
705 rich magma that suppressed the water content, and the 2014 explosive eruption was driven by
706 water saturated magma. On the other hand, Jeffery et al. (2013) invoked additional processes
707 such as crustal contamination, inter-crustal magma mixing, xenolith incorporation, and magma
708 migration, where the volatile content degassed from 8 wt. % to 2-3 wt. % during magma
709 migration. We have as yet no definitive geochemical or textural evidence to suggest that magma
710 mixing is a dominant process at Kelud based on mineral chemistry and textures interpretations
711 presented in Utami et al. (in revision).
712
713

714 **Table 11.** *Excess volatile estimates for the 2014 magma using the petrologic method of Devine et*
715 *al. (1984).*
716

	14-PUMI-2	Units
Erupted volume (DRE)[a]	0.28	km^3
Rock density	2404	kg/m^3
Mass of magma	673	Mt
Max. concentration of SO_2 in melt inclusion	547-582	ppm
Max concentration of SO_2 in interstitial glass	95-126	ppm
Glass proportion	0.66-0.71	
SO_2 degassed from the melt	0.20-0.22	Mt
Atmospheric SO_2[b]	0.30	Mt
Excess SO_2	0.08-0.10	Mt

717
718 *Notes*. [a]Erupted volume from Maeno et al. (2019). [b]SO_2 from Carn (2019).
719

720 The accumulation of an excess fluid also requires that the plumbing system behaves as a
721 closed system, or with the mass flux of exsolved fluids that was produced being larger than that
722 which is degassed, implies that there was limited passive degassing between eruptions. Kelud
723 volcano is considered semi-plugged by Whelley et al. (2015). Prior to 1990 eruption, degassing
724 from depth was likely blocked by a plug of crystalline magma from the previous event in 1966
725 and ~4 million m^3 of lake water (Lesage & Surono, 1995; Vandemeulebrouck et al., 2000),
726 whereas before the 2014 eruption, the volcano was plugged by the 2007 dome (Global
727 Volcanism Program, 2014). The 1990 plug and 2007 dome likely provided little permeability for
728 the fluids to escape, in addition to exerting relatively high lithostatic/hydrostatic pressure. These
729 conditions could have effectively decreased the rock's permeability and allowed fluids and
730 overpressure to accumulate before eruption. Minerals such as cristobalite likely formed at
731 shallow pressures (< 50 MPa) during and after dome emplacement and contribute reducing the
732 permeability of the dome (Horwell et al., 2013; Martel & Schmidt, 2003). In contrast, after the
733 1990 eruption and up until 2007, there was significant outgassing from arcuate fractures
734 observed, and an "embryonic" dome sealed the conduit (Global Volcanism Program, 1990b).
735 The observed fumarolic activity and outgassing likely stemmed from active degassing of a
736 shallow magma body from a residual magma intrusion, similar to a resurgent dome (Acocella et
737 al., 2000; Global Volcanism Program, 1990b). Between 1990 and 2007, there were also several
738 crises involving two heating episodes, when the lake water increased in temperature from 40°C
739 and 35°C in 1996 and 2001, respectively to ~50°C (Bernard & Mazot, 2004). The observed post-

and inter-eruptive crises between 1990 to 2007 suggest the magma system was partially open, allowing the shallow magma body to further degas volatiles out of the system and thus was not able to accumulate a significant amount of excess fluids.

5.3 Relating pre-eruptive processes to unrest signals

Volcanic unrest at Kelud has been monitored using a range of observations, including seismicity, lake chemistry and its temperature, and deformation. Unrest signals preceding all three events started around 2-3 months before eruption, and included seismic swarms with seismic unrest signals spanning volcano-tectonic, shallow VB, low frequency, tremor (e.g. Hidayati, 2009; Hidayati et al., 2018; Lesage & Surono, 1995). Seismicity escalated rapidly (e.g. < 24 hours) before the 1990 and 2014 eruptions, and earthquake hypocenters are mostly concentrated around shallow depths beneath the crater (< 7 km) (Hidayati et al., 2018; Lesage & Surono, 1995). Sharp increases in lake temperature and input of magmatic volatiles such as Cl_2 and CO_2 into the lake have also been proposed for the unrest prior to the 1990 and 2007 eruptions (Bernard & Mazot, 2004; Caudron et al., 2012; Kunrat, 2009; Vandemeulebrouck et al., 2000). Tiltmeters and interferometric synthetic aperture radar (InSAR) detected changes in local and regional deformation from inflation to rapid deflation preceding 2014 eruption and 2007 dome extrusion, respectively (Hidayati et al., 2018; Lubis, 2014). Despite the diverse monitoring data available, it is still difficult to anticipate eruptions at Kelud, including whether the ensuing eruption will be effusive or explosive (Nakamichi et al., 2017).

Results of our study suggest that the accumulation of an excess volatile phase prior to the eruptions of 1990 and 2014 was a key parameter to their explosivity (Fig. 7). Contrasting this with the inter-eruptive period between the 1990 and 2007, where the system was able to degas more freely, which then resulted in the 2007 eruption being effusive. If our hypothesis is correct, identifying monitoring signals that could be related to fluid accumulation and magma degassing or transfer within the plumbing system could be useful in anticipating explosive eruptions. One possibility is to monitor deep long period seismicity using broadband seismometers as this has been interpreted as degassing of volatile-rich magma at depth (Melnik et al., 2020). Another possibility are microgravity surveys or continuous gravity monitoring, as we can expect that

significant fluid accumulation would lead to subtle changes in density of the plumbing system over time, as demonstrated in Masaya volcano (Nicaragua) (e.g. Williams-Jones et al., 2003).

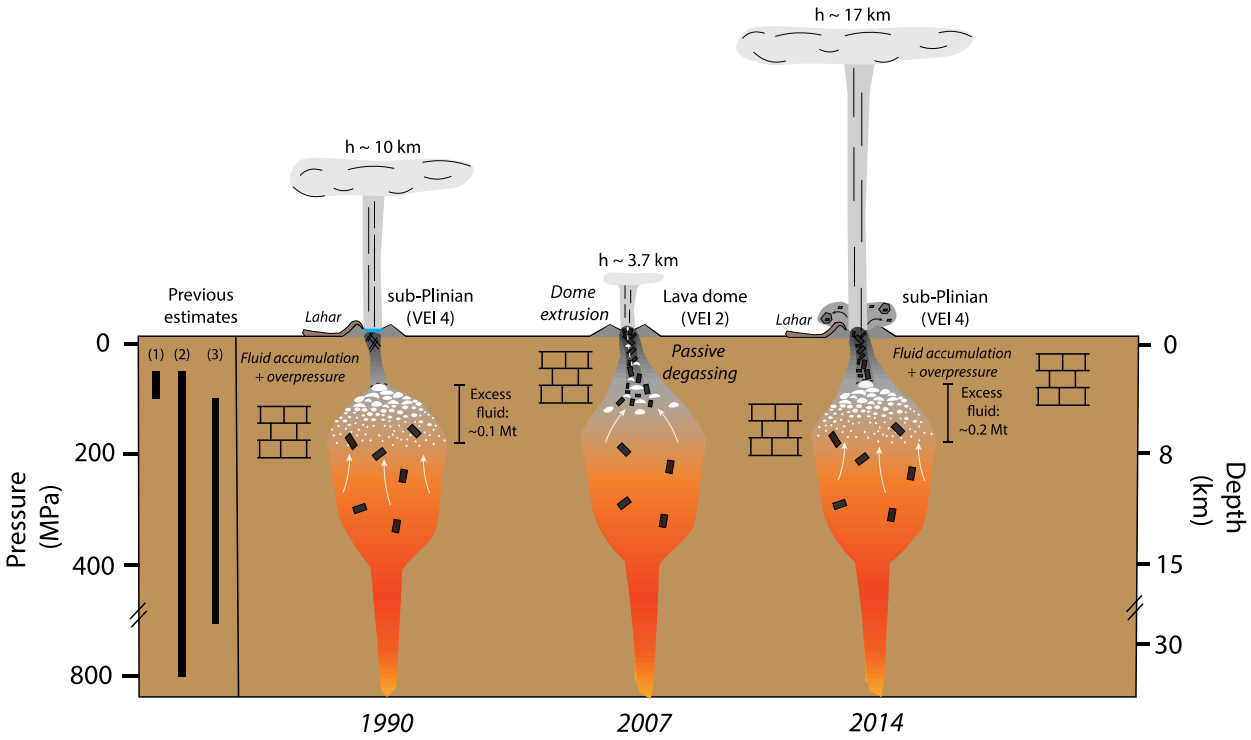

Figure 7. *Conceptual model of the magmatic conditions and processes occurring for the 1990-2014 Kelud eruptions. Black rectangles represent the crystal cargo, or crystallization in the conduit. White flattened circles represent accumulation of the pre-eruptive excess fluid phase present before explosive eruptions. Solid white arrows represent fluid fluxing through the system either from a deep-seated degassing basaltic magma, or from limestone assimilation. Dashed white arrows represent fluid release through a semi-permeable conduit leading up to dome extrusion. The 1990 and 2014 magmas were able to accumulate an excess volatile phase and hence the higher explosivity of their eruptions, where as a higher permeability of the system between 1990 and 2007 allowed for extended degassing and slower ascent of the 2007 as a dome. Pressures are converted to depth below the crater using the density calculated in Smyth et al. (2007). The volcaniclastic and carbonate layers are also in Smyth et al. (2007), as represented in Jeffery et al. (2013). Volcano Explosivity Indices (VEI) reported come from Global Volcanism Program (2013). Storage depth constraints come from Cassidy et al. (2019)*

(2014 eruption) [1], Jeffery et al. (2013) (2007 dome) [2], and Utami et al. (in revision) (1990 eruption) [3]. Plume height were reported in Bourdier et al. (1997) for 1990; Global Volcanism Program (2008) for 2007; and Kristiansen et al. (2015) for 2014.

6 Conclusions

We present petrological and experimental constraints on the pre-eruptive storage conditions of the basaltic andesite magma feeding the 1990, 2007, and 2014 eruptions of Kelud volcano, which alternated between explosive → effusive → explosive eruption styles. The three events share similar whole rock compositions, mineralogy, implying that their magma storage conditions were also similar. We found that the natural phenocryst conten and mineral assemblage can be experimentally reproduced at 975 ± 39°C, 175 ± 25 MPa (~7 km below the crater level), NNO, and with 4-6 wt. % water in the melt. We also found that the 1990 and 2014 magmas coexisted with an exsolved volatile phase at pre-eruptive conditions, and we propose that this played a main role to their explosive style. The lava dome was likely a residual magma batch from the 1990 eruption or earlier that had no excess fluids, as the conduit was partially open after the 1990 eruption that allowed gases to be released. Monitoring techniques such as continuous microgravity surveys could help to identify changes in density from fluid accumulation and thus may be able to anticipate eruption styles.

7 Acknowledgments

We would like to thank R. Champallier and I. di Carlo from ISTO-Orléans for assistance with experiments and sensor analyses. Hsu Y-J, J. Herrin, and J. Oalmann from the Earth Observatory of Singapore are thanked for assistance with analyses on the SEM, EPMA, and discussions around experimental petrology. We would like to acknowledge the Facility for Analysis, Characterisation, Testing and Simulation, Nanyang Technological University, Singapore, for use of their electron microscopy/X-ray facilities. We further thank C. Widiwijayanti, P. Lesage, and P. Allard for discussions on Kelud volcano. We thank S. Jenkins for being part of the thesis advisory committee. This project was funded by the Stephen Riady Geosciences Scholarship 2018-2019 awarded to SBU. The data underlying this project are

available at DR-NTU (https://researchdata.ntu.edu.sg/privateurl.xhtml?token=6981d93f-ea77-4057-88e2-19c0480fa99e), and available as online supplementary material (Datasets S1 and S2).

We are in the process of archiving our data. There are no financial conflicts of interests between any author.

8 References

Acocella, V., Cifelli, F., & Funiciello, R. (2000). Analogue models of collapse calderas and resurgent domes. *Journal of Volcanology and Geothermal Research*, *104*(1), 81–96. https://doi.org/https://doi.org/10.1016/S0377-0273(00)00201-8

Arzilli, F., Morgavi, D., Petrelli, M., Polacci, M., Burton, M., Di Genova, D., Spina, L., La Spina, G., Hartley, M. E., Romero, J. E., Fellowes, J., Diaz-Alvarado, J., & Perugini, D. (2019). The unexpected explosive sub-Plinian eruption of Calbuco volcano (22–23 April 2015; southern Chile): Triggering mechanism implications. *Journal of Volcanology and Geothermal Research*, *378*(April 2015), 35–50. https://doi.org/10.1016/j.jvolgeores.2019.04.006

Bernard, A., Knittel, U., Weber, B., Weis, D., Albrecht, A., Hattori, K., Klein, J., & Oles, D. (1996). Petrology and geochemistry of the 1991 eruption products of Mount Pinatubo. In C. G. Newhall & R. S. Punongbayan (Eds.), *FIRE and MUD: Eruptions and Lahars of Mount Pinatubo, Philippines*. Univ of Washington Press.

Bernard, A., & Mazot, A. (2004). Geochemical evolution of the young crater lake of Kelud volcano in Indonesia. In R. R. S. I. I. R.B. Wanty (Ed.), *Water-Rock Interaction (WRI-11)* (pp. 87–90). A.A. Balkema.

Bourdier, J. L., Pratomo, I., Thouret, J. C., Boudon, G., & Vincent, P. M. (1997). Observations, stratigraphy and eruptive processes of the 1990 eruption of Kelut volcano, Indonesia. *Journal of Volcanology and Geothermal Research*, *79*(3), 181–203.

Bucholz, C. E., Gaetani, G. A., Behn, M. D., & Shimizu, N. (2013). Post-entrapment modification of volatiles and oxygen fugacity in olivine-hosted melt inclusions. *Earth and Planetary Science Letters*, *374*, 145–155. https://doi.org/10.1016/j.epsl.2013.05.033

Bull, K. F., & Buurman, H. (2013). An overview of the 2009 eruption of Redoubt Volcano, Alaska. *Journal of Volcanology and Geothermal Research*, *259*(March 2009), 2–15. https://doi.org/10.1016/j.jvolgeores.2012.06.024

Caricchi, L., Sheldrake, T. E., & Blundy, J. (2018). Modulation of magmatic processes by CO2 flushing. *Earth and Planetary Science Letters*, *491*, 160–171. https://doi.org/10.1016/j.epsl.2018.03.042

Cashman, K. V., Stephen, R., & Sparks, J. (2013). How volcanoes work: A 25 year perspective. *Bulletin of the Geological Society of America*, *125*(5–6), 664–690. https://doi.org/10.1130/B30720.1

Cassidy, M., Castro, J. M., Helo, C., Troll, V. R., Deegan, F. M., Muir, D., Neave, D. A., & Mueller, S. P. (2016). Volatile dilution during magma injections and implications for volcano explosivity. *Geology*, *44*(12), 1027–1030.

Cassidy, M., Ebmeier, S. K., Helo, C., Watt, S. F. L., Caudron, C., Odell, A., Spaans, K., Kristianto, P., Triastuty, H., Gunawan, H., & Castro, J. M. (2019). Explosive Eruptions With Little Warning: Experimental Petrology and Volcano Monitoring Observations From the 2014 Eruption of Kelud, Indonesia. *Geochemistry, Geophysics, Geosystems*, 1–30. https://doi.org/10.1029/2018gc008161

Cassidy, M., Manga, M., Cashman, K., & Bachmann, O. (2018). Controls on explosive-effusive volcanic eruption styles. *Nature Communications*, *9*(1). https://doi.org/10.1038/s41467-018-05293-3

Caudron, C., Mazot, A., & Bernard, A. (2012). Carbon dioxide dynamics in Kelud volcanic lake. *Journal of Geophysical Research: Solid Earth*, *117*(B5).

Deer, W. A., Howie, R. A., & Zussman, J. (1992). *An introduction to the rock-forming minerals* (2nd ed.). Longman Scientific & Technical.

Devine, D., Siggurdson, H., & Davis, A. N. (1984). Estimates of sulfur and chlorine yield to the atmosphere from volcanic eruptions and potential climatic effects. *Journal of Geophysical Research*, *89*(B7), 6309–6325.

Dingwell, D. B., Bagdassarov, N. S., Bussod, G. Y., & Webb, S. L. (1993). Magma Rheology. In R. W. Luth (Ed.), *Experiments at High Pressure and Applications to the Earth's Mantle: Short Course Handbook* (Volume 21, pp. 131–196). Mineralogical Association of Canada.

Elissondo, M., Baumann, V., Bonadonna, C., Pistolesi, M., Cioni, R., Bertagnini, A., Biass, S., Herrero, J. C., & Gonzalez, R. (2016). Chronology and impact of the 2011 Cordón Caulle eruption, Chile. *Natural Hazards and Earth System Sciences*, *16*(3), 675–704. https://doi.org/10.5194/nhess-16-675-2016

Erdmann, S., Martel, C., Pichavant, M., Bourdier, J.-L., Champallier, R., Komorowski, J.-C., & Cholik, N. (2016). Constraints from phase equilibrium experiments on pre-eruptive storage conditions in mixed magma systems: A case study on crystal-rich basaltic andesites from Mount Merapi, Indonesia. *Journal of Petrology*, *57*(3), 535–560.

Giordano, D., Russell, J. K., & Dingwell, D. B. (2008). Viscosity of magmatic liquids: a model. *Earth and Planetary Science Letters*, *271*(1), 123–134.

Giuffrida, M., Holtz, F., Vetere, F., & Viccaro, M. (2017). Effects of CO2flushing on crystal textures and compositions: experimental evidence from recent K-trachybasalts erupted at Mt. Etna. *Contributions to Mineralogy and Petrology*, *172*(11–12), 1–18. https://doi.org/10.1007/s00410-017-1408-3

Global Volcanism Program, G. V. P. (1990a). Report on Kelut (Indonesia). *Bulletin of the Global Volcanism Network*, *15*(1). https://doi.org/10.5479/si.GVP.BGVN199001-263280

Global Volcanism Program, G. V. P. (1990b). *Report on Kelut (Indonesia)*. *15*(9).

Global Volcanism Program, G. V. P. (2007). Report on Kelut (Indonesia). *Bulletin of the Global Volcanism Network*, *31*.

Global Volcanism Program, G. V. P. (2008). *Report on Kelut (Indonesia)*. *33*(7). https://doi.org/10.5479/si.GVP.BGVN200807-263280

Global Volcanism Program, G. V. P. (2013). *Kelut (Kelud)*.

https://doi.org/10.5479/si.GVP.VOTW4-2013

Global Volcanism Program, G. V. P. (2014). *Report on Kelut (Indonesia)*. *39*(2). https://doi.org/10.5479/si.GVP.BGVN201402-263280

Gonnermann, H. M., & Manga, M. (2013). Dynamics of magma ascent in the volcanic conduit. In S. Fagents, T. K. P. Gregg, & R. M. C. Lopes (Eds.), *Modeling Volcanic Processes: The Physics and Mathematics of Volcanism* (Vol. 9780521895, pp. 55–84). Cambridge University Press. https://doi.org/10.1017/CBO9781139021562.004

Hidayati, S. (2009). Emergence of Lava Dome from the Crater Lake of Kelud Volcano, East Java. *Indonesian Journal on Geoscience*, *4*(4), 229–238. https://doi.org/10.17014/ijog.vol4no4.20091

Hidayati, S., Basuki, A., Kristianto, & Mulyana, I. (2009). *Emergence of Lava Dome from the Crater Lake of Kelud Volcano , East Java*. *4*(4), 229–238.

Hidayati, S., Triastuty, H., Mulyana, I., Adi, S., Ishihara, K., Basuki, A., Kuswandarto, H., Priyanto, B., & Solikhin, A. (2018). Differences in the seismicity preceding the 2007 and 2014 eruptions of Kelud volcano, Indonesia. *Journal of Volcanology and Geothermal Research*, *xxxx*. https://doi.org/10.1016/j.jvolgeores.2018.10.017

Horwell, C. J., Williamson, B. J., Llewellin, E. W., Damby, D. E., & Le Blond, J. S. (2013). The nature and formation of cristobalite at the Soufrière Hills volcano, Montserrat: Implications for the petrology and stability of silicic lava domes. *Bulletin of Volcanology*, *75*(3), 1–19. https://doi.org/10.1007/s00445-013-0696-3

Humaida, H. (2013). *A geochemical study on Merapi and Kelud volcanic eruptions.* Universitas Gadjah Mada.

Jeffery, A. J., Gertisser, R., Troll, V. R., Jolis, E. M., Dahren, B., Harris, C., Tindle, A. G., Preece, K., O'Driscoll, B., Humaida, H., & others. (2013). The pre-eruptive magma plumbing system of the 2007--2008 dome-forming eruption of Kelut volcano, East Java, Indonesia. *Contributions to Mineralogy and Petrology*, *166*(1), 275–308.

Kristiansen, N. I., Prata, A. J., Stohl, A., & Carn, S. A. (2015). Stratospheric volcanic ash emissions from the 13 February 2014 Kelut eruption. *Geophysical Research Letters*, *42*(2), 588–596.

Kunrat, S. L. (2009). *Geochemical and Thermodynamic Modeling of Volcanic Fluids and Their Interpretation for Volcano Monitoring*. Universite Libre de Bruxelles.

Leake, B. E., Woolley, A. R., Arps, C. E. ., Birch, W. D., Gilbert, M. C., Grice, J. D., Hawthorne, F. C., Kato, A., Kisch, H. J., Krivovichev, V. G., Linthout, K., Laird, J., Maresch, W. V., Nickel, E. H., Rock, N. M. ., Schumacher, J. C., Smith, D. C., Stephenson, N. C. N., Ungaretti, L., … G., Y. (1997). Nomenclature of amphiboles Report of the Subcommittee on Amphiboles of the International Mineralogical Association Commission on New Minerals and Mineral Names. *Canadian Mineralogist*, *9*, 623–651.

Lesage, P., & Surono. (1995). Seismic precursors of the February 10, 1990 eruption of Kelut volcano, Java. *Journal of Volcanology and Geothermal Research*, *65*(1), 135–146.

Lubis, A. M. (2014). Uplift of Kelud Volcano Prior to the November 2007 Eruption as Observed by L-Band Insar. *Journal of Engineering and Technological Sciences*, *46*(3), 245–257.

Maeno, F., Nakada, S., Yoshimoto, M., Shimano, T., Hokanishi, N., Zaennudin, A., & Iguchi, M. (2019). Eruption pattern and a long-term magma discharge rate over the past 100 years at Kelud Volcano, Indonesia. *Journal of Disaster Research*, *14*(1), 27–39. https://doi.org/10.20965/JDR.2019.P0027

Martel, C., & Schmidt, B. C. (2003). *Decompression experiments as an insight into ascent rates of silicic magmas*. 397–415. https://doi.org/10.1007/s00410-002-0404-3

Melnik, O., Lyakhovsky, V., Shapiro, N. M., Galina, N., & Bergal-Kuvikas, O. (2020). Deep long period volcanic earthquakes generated by degassing of volatile-rich basaltic magmas. *Nature Communications*, *11*(1), 1–7. https://doi.org/10.1038/s41467-020-17759-4

Nakamichi, H., Iguchi, M., Triastuty, H., Hendrasto, M., & Mulyana, I. (2017). Differences of precursory seismic energy release for the 2007 effusive dome-forming and 2014 Plinian eruptions at Kelud volcano, Indonesia. *Journal of Volcanology and Geothermal Research*. https://doi.org/10.1016/j.jvolgeores.2017.08.004

Nakashima, Y., Heki, K., Takeo, A., Cahyadi, M. N., Aditiya, A., & Yoshizawa, K. (2016). Atmospheric resonant oscillations by the 2014 eruption of the Kelud volcano, Indonesia, observed with the ionospheric total electron contents and seismic signals. *Earth and Planetary Science Letters*, *434*, 112–116. https://doi.org/10.1016/j.epsl.2015.11.029

Norrish, K., & Hutton, J. T. (1969). An accurate X-ray spectrographic method for the analysis of a wide range of geological samples. *Geochimica et Cosmochimica Acta*, *33*(4), 431–453.

Pallister, J. S., Hoblitt, R. P., Crandell, D. R., & Mullineaux, D. R. (1992). Mount St. Helens a decade after the 1980 eruptions: magmatic models, chemical cycles, and a revised hazards assessment. *Bulletin of Volcanology*, *54*, 126–146.

Pallister, J. S., Hoblitt, R. P., Meeker, G. P., Knight, R. J., & Siems, D. F. (1996). Magma Mixing at Mount Pinatubo: Petrographic and Chemical Evidence from the 1991 Deposits. In C. G. Newhall & R. S. Punongbayan (Eds.), *FIRE and MUD: Eruptions and Lahars of Mount Pinatubo, Philippines*. Univ of Washington Press.

Pardyanto, L. (1990). *Laporan Letusan Kelut 10 Februari 1990*.

Pichavant, M., Martel, C., Bourdier, J.-L., & Scaillet, B. (2002). Physical conditions, structure, and dynamics of a zoned magma chamber: Mount Pelée (Martinique, Lesser Antilles Arc). *Journal of Geophysical Research*, *107*(B5). https://doi.org/10.1029/2001jb000315

Prouteau, G., & Scaillet, B. (2003). Experimental Constraints on the Origin of the 1991 Pinatubo Dacite. *Journal of Petrology*, *44*(12), 2203–2241. https://doi.org/10.1093/petrology/egg075

Putirka, K. D. (2008). Thermometers and barometers for volcanic systems. *Reviews in Mineralogy and Geochemistry*, *69*(1), 61–120.

Ridolfi, F., Renzulli, A., & Puerini, M. (2010). Stability and chemical equilibrium of amphibole in calc-alkaline magmas: an overview, new thermobarometric formulations and application to subduction-related volcanoes. *Contributions to Mineralogy and Petrology*, *160*(1), 45–66.

Roux, J., & Lefèvre, A. (1992). A fast-quench device for internally heated pressure vessels. *European Journal of Mineralogy*, *4*(2), 279–282. https://doi.org/10.1127/ejm/4/2/0279

977 Scaillet, B., Clemente, B., Evans, B. W., & Pichavant, M. (1998). Redox control of sulfur
978 degassing in silicic magmas the from. *Journal of Geophysical Research*, *103*(98), 937–949.

979 Scaillet, B., & Evans, B. W. (1999). The 15 June 1991 eruption of Mount Pinatubo. I. Phase
980 equilibria and pre-eruption P-T-fO 2 -fH 2 O conditions of the dacite magma. *Journal of*
981 *Petrology*, *40*(3), 381–411. https://doi.org/10.1093/petroj/40.3.381

982 Scaillet, B., Pichavant, M., & Roux, J. (1995). Experimental Crystallization of Leucogranite
983 Magmas. *Journal of Petrology*, *36*(3), 663–705.

984 Scaillet, B., Pichavant, M., Roux, J., Humbert, G., & Lefevre, A. (1992). Improvements of the
985 Shaw membrane technique for measurement and control of fH2 at high temperatures and
986 pressures. *American Mineralogist*, *77*(5–6), 647–655.

987 Shinohara, H. (2008). Excess degassing from volcanoes and its role on eruptive and intrusive
988 activity. *Reviews of Geophysics*, *46*(4), 1–31. https://doi.org/10.1029/2007RG000244

989 Shishkina, T. A., Botcharnikov, R. E., Holtz, F., Almeev, R. R., & Portnyagin, M. V. (2010).
990 Solubility of H2O- and CO2-bearing fluids in tholeiitic basalts at pressures up to 500MPa.
991 *Chemical Geology*, *277*(1–2), 115–125. https://doi.org/10.1016/j.chemgeo.2010.07.014

992 Sisson, T. W., & Bacon, C. R. (1999). Gas-driven filter pressing in magmas. *Geology*, *27*(7),
993 613–616. https://doi.org/10.1130/0091-7613(1999)027<0613:GDFPIM>2.3.CO;2

994 Surono, Jousset, P., Pallister, J., Boichu, M., Buongiorno, M. F., Budisantoso, A., Costa, F.,
995 Andreastuti, S., Prata, F., Schneider, D., Clarisse, L., Humaida, H., Sumarti, S., Bignami,
996 C., Griswold, J., Carn, S., Oppenheimer, C., & Lavigne, F. (2012). The 2010 explosive
997 eruption of Java's Merapi volcano-A "100-year" event. *Journal of Volcanology and*
998 *Geothermal Research*, *241–242*, 121–135. https://doi.org/10.1016/j.jvolgeores.2012.06.018

999 Taylor, J. R., Wall, V. J., & Pownceby, M. I. (1992). The calibration and application of accurate
1000 redox sensors. *American Mineralogist*, *77*(3–4), 284–295.

1001 Thouret, J.-C., Abdurachman, K. E., Bourdier, J.-L., & Bronto, S. (1998). Origin, characteristics,
1002 and behaviour of lahars following the 1990 eruption of Kelud volcano, eastern Java
1003 (Indonesia). *Bulletin of Volcanology*, *59*(7), 460–480.

1004 Tramontano, S., Gualda, G. A. R., & Ghiorso, M. S. (2017). Internal triggering of volcanic
1005 eruptions: tracking overpressure regimes for giant magma bodies. *Earth and Planetary*
1006 *Science Letters*, *472*, 142–151. https://doi.org/10.1016/j.epsl.2017.05.014

1007 Vandemeulebrouck, J., Sabroux, J.-C., Halbwachs, M., Poussielgue, N., Grangeon, J., Tabbagh,
1008 J., & others. (2000). Hydroacoustic noise precursors of the 1990 eruption of Kelut Volcano,
1009 Indonesia. *Journal of Volcanology and Geothermal Research*, *97*(1), 443–456.

1010 Waters, L. E., & Lange, R. A. (2015). An updated calibration of the plagioclase-liquid
1011 hygrometer-thermometer applicable to basalts through rhyolites. *American Mineralogist*,
1012 *100*(10), 2172–2184.

1013 Waters, L. E., & Lange, R. A. (2017). An experimental study of Fe2+-MgKD between
1014 orthopyroxene and rhyolite: a strong dependence on H2O in the melt. *Contributions to*
1015 *Mineralogy and Petrology*, *172*(6), 1–13. https://doi.org/10.1007/s00410-017-1358-9

1016 Whelley, P. L., Newhall, C. G., & Bradley, K. E. (2015). The frequency of explosive volcanic

eruptions in Southeast Asia. *Bulletin of Volcanology*, *77*(1). https://doi.org/10.1007/s00445-014-0893-8

Williams-Jones, G., Rymer, H., & Rothery, D. A. (2003). Gravity changes and passive SO2 degassing at the Masaya caldera complex, Nicaragua. *Journal of Volcanology and Geothermal Research*, *123*(1–2), 137–160. https://doi.org/10.1016/S0377-0273(03)00033-7

Wirakusumah, A. D. (1991). *Some studies of volcanology, petrology and structure of Mt. Kelut, east Java, Indonesia*. Victoria University of Wellington.

Young, S. R., Sparks, R. S. J., Aspinall, W. P., Lynch, L. L., Miller, A. D., Robertson, R. E. A., & Shepherd, J. B. (1998). Overview of the eruption of Soufriere Hills Volcano, Montserrat, 18 July 1995 to December 1997. *Geophysical Research Letters*, *25*(18), 3389–3392. https://doi.org/10.1029/98GL01405